STUDYING THE Au/Si(100) SYSTEM USING THE MODIFIED EMBEDDED ATOM METHOD

LU YAO

Your file Votre référence
ISBN: 978-0-494-33456-0
Our file Notre référence
ISBN: 978-0-494-33456-0

Studying the Au/Si(100) System using the Modified Embedded Atom Method

by

© Lu Yao
Master of Science

A thesis submitted to the
Department of Physics and Physical Oceanography
in partial fulfillment of the
requirements for the degree of
Master of Science.

Department of Physics and Physical Oceanography
Memorial University of Newfoundland

August 31, 2007

St. John's Newfoundland

Abstract

Molecular dynamics simulations based on the modified embedded atom method were applied to study the formation of thin Au films on the Si(100) substrate. Different Au coverages were used to study how the Au concentration affected the structure and morphology of the thin Au film on the Si substrate. It was found that Au atoms re-evaporated from the Si surface below 1 ML coverage at room temperature, and became more stable when the coverage was increased. Above 1 ML, all the Au atoms stayed on the Si substrate without re-evaporation. In our simulations, no Au/Si intermixing was observed within the simulation time of 41.25 ps below 3 ML Au coverage at room temperature. We also calculated the surface stress as the system evolved with time. The calculations showed the surface stress oscillated intensively at the beginning of the simulations and became stable when the system approached equilibrium. Comparing the surface stress of the system at different Au coverages, we found that the surface stress became smaller when the Au coverage was increased. Lastly, we studied the influence of temperature on the Au/Si interactions. Our results showed Au and Si intermixed above 2 ML Au coverage at 800 K, indicating that the Au/Si interactions could be enhanced by increasing the temperature.

Acknowledge

This thesis would not have been possible without help and support from many people. I would like to express my gratitude here.

First of all, I would like to sincerely thank my supervisor Dr.Beaulieu who has been so supportive, helpful, and patient during this program. Without his instruction and inspiration, this thesis would have never been written. I owe him lots of gratitude not only for his guidance in my research but also for his kindness and encouragement all the time. His active involvement with students and sense of humor made working with him really enjoyable. I never had a supervisor as kind as him, and I do not expect I will in the future.

I would like to thank John Braeckmann who wrote the original programs and set the foundation for this thesis work. I would also like to thank Mike Coates in my group who wrote a Visual Basic program which facilitated analyzing my data. I would like to thank Mark S. Staveley (Regional Research Associate of ACEnet) and Fred Perry (Systems Administrator in Physics Department) for helping me using the ACEnet machines, and Dr.Plumer for letting me use his account of the workstation when I had an urgent need for running the jobs. I would like to thank Dr.Saika-Voivod and Jason Mercer for their advice and friendly help which were valuable for my thesis study. I would also like to thank Dr.Andrews and Dr.Poduska for recommending very helpful references about the surface stress and thin film preparation.

Finally, I want to thank my parents who gave me birth and strength. Thank you for your unconditional love, support and confidence in me during my growth. I would also like to thank all my friends who are always there helping me to build confidence

in front of any difficulties and offering companionship which made me have a really good time in these two years. Thank you for giving me so many beautiful memories and getting me to know how precious friendship can be in one's life time.

Contents

List of Tables

List of Figures

Chapter 1

Introduction

1.1 Motivation

Micro-cantilever sensors are good candidates for molecular detection devices. Made from silicon, these cantilevers are typically between 200-300 μm in length, 30-50 μm in width and 0.5-1 μm in thickness. Owing to their small size, cantilever sensors are extremely sensitive to changes of mechanical properties such as surface stress. It has been reported that the sensitivity of a cantilever can be at the nanogram (10^{-9}), picoliter (10^{-12}), femtojoule (10^{-15}), and attomolar (10^{-18}) scales, and the response time can be less than milliseconds [1].

Figure 1.1: Deflection of the cantilever due to change of surface stress in molecular detection.

In static mode, the molecular detection event can be identified as a cantilever deflection. When molecules adsorb on one side of the cantilever, a change in surface stress causes the cantilever to bend downwards as shown in Figure 1.1. The cantilever deflection can be measured by a laser beam reflected from the apex of the cantilever into a position sensitive detector as shown in Figure 1.2. When the laser beam is reflected, the displacement of the reflected spot is proportional to the cantilever deflection; therefore, using a photodetector which detects the displacement of the reflected spot, deflection of the cantilever can be monitored.

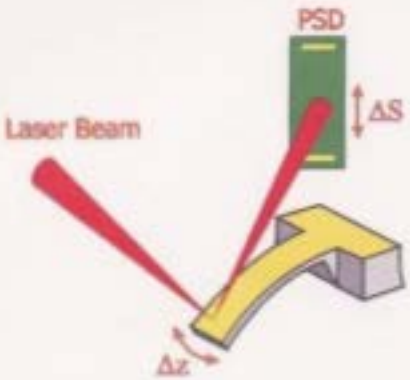

Figure 1.2: The deflection of a cantilever is monitored using the optical beam deflection method.(Drawn by Michel Godin)

Cantilever sensors have been used to study the adsorption of self-assembled monolayers. The IBM group first performed studies of the adsorption of alkanethiol molecules on gold-coated micro-cantilevers [2]. Alkanethiols ($HS(CH_2)_nCH_3$) are hydrocarbon chains with a sulfur atom at one end as shown in Figure 1.3(b), in which the red sphere denotes the S atom while the rest shows the hydrocarbon chain of the molecule. These molecules form well defined, strongly bonded self-assembled monolayers (SAM) on gold. Figure 1.3(a) shows alkanethiols binding to a gold-coated cantilever forming a self-assembled monolayer. The SAM causes a change in surface stress of the Au film which in turn causes the cantilever to bend. The solid red lines in Figure 1.3(a) represent the incident and reflected laser beams used to monitor the deflection of the cantilever.

In static mode, the molecular detection event can be identified as a cantilever deflection. When molecules adsorb on one side of the cantilever, a change in surface stress causes the cantilever to bend downwards as shown in Figure 1.1. The cantilever deflection can be measured by a laser beam reflected from the apex of the cantilever into a position sensitive detector as shown in Figure 1.2. When the laser beam is reflected, the displacement of the reflected spot is proportional to the cantilever deflection; therefore, using a photodetector which detects the displacement of the reflected spot, deflection of the cantilever can be monitored.

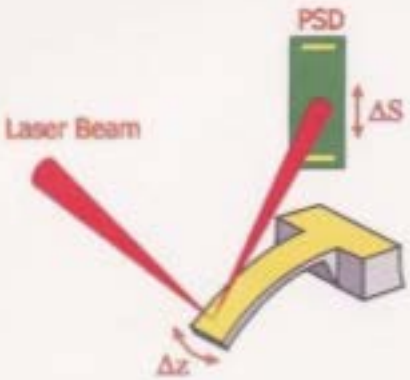

Figure 1.2: The deflection of a cantilever is monitored using the optical beam deflection method.(Drawn by Michel Godin)

Cantilever sensors have been used to study the adsorption of self-assembled monolayers. The IBM group first performed studies of the adsorption of alkanethiol molecules on gold-coated micro-cantilevers [2]. Alkanethiols ($HS(CH_2)_nCH_3$) are hydrocarbon chains with a sulfur atom at one end as shown in Figure 1.3(b), in which the red sphere denotes the S atom while the rest shows the hydrocarbon chain of the molecule. These molecules form well defined, strongly bonded self-assembled monolayers (SAM) on gold. Figure 1.3(a) shows alkanethiols binding to a gold-coated cantilever forming a self-assembled monolayer. The SAM causes a change in surface stress of the Au film which in turn causes the cantilever to bend. The solid red lines in Figure 1.3(a) represent the incident and reflected laser beams used to monitor the deflection of the cantilever.

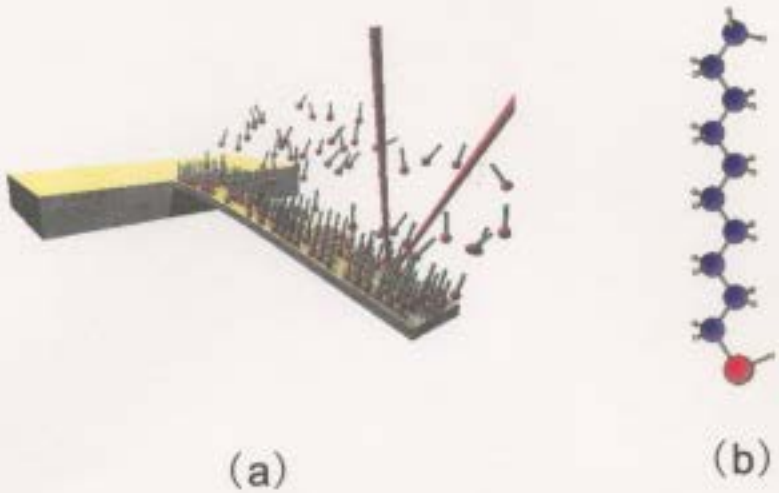

Figure 1.3: Self-assembled monolayer on the gold-coated cantilever. (a) Formation of the self-assembled monolayer when the alkanethiols bind to a gold-coated cantilever. (b) Structure of the alkanethiol molecule.

After the IBM work it was shown by Godin *et al.* that the response of cantilever sensors to alkanethoils depends on the morphology of the gold film [3]. In their study, two types of gold films were prepared: one with a relatively small average grain size, and the other with a large average grain size. Figure 1.4 shows STM images of these two gold films. These two types of gold on cantilevers were then exposed to alkanethiols and the deflection and surface stress were measured. Figure 1.5 shows the deflection (left ordinate) and surface stress (right ordinate) as a function of time as alkanethiols adsorbed on the two gold-coated cantilevers with two different morphologies. The red curve shows the deflection and surface stress of a small grain gold-coated cantilever while the black curve shows the deflection and surface stress of a large grain gold-coated cantilever as they react with alkanethiols. As can be seen, the cantilever with large grain gold underwent a much larger deflection than the cantilever with small grain gold. We can also see that the SAM grown on large-

grained gold exhibits a long-term increase in surface stress, which is not observed for the SAM grown on small-grained gold.

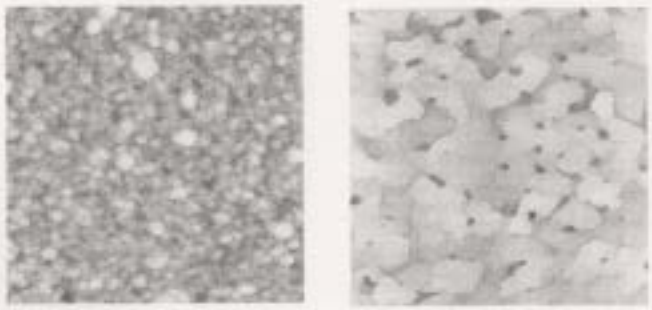

Figure 1.4: STM images (3 μm $\times$ 3 μm) of (A) large-grained gold and (B) small-grained gold. These STM images were obtained by Godin *et. al.* at McGill university [3].

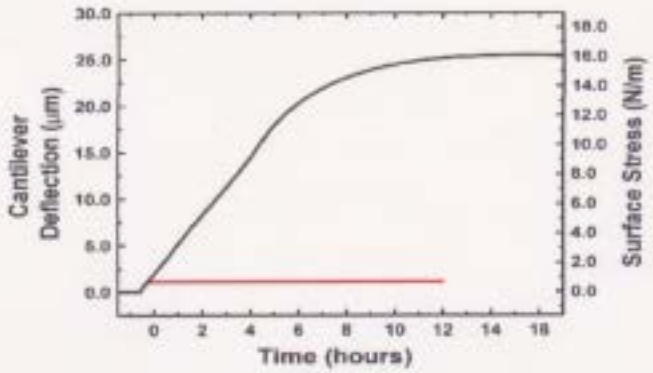

Figure 1.5: The cantilever deflection and surface stress induced during the formation of the SAM on gold-coated cantilevers. This graph was obtained by Godin *et. al.* at McGill university [3].

Therefore, since the sensitivity of the cantilever sensors depends on the morphology of the top Au film, it is important to understand the deposition process of gold on the silicon cantilevers. Deposition of gold on silicon substrate has been investigated by many groups; however, there are significant disagreements on the experimental

results among different groups [4-17]. To understand what influences the morphology of gold on silicon, we have written a program based on the Modified Embedded Atom Method (MEAM) to conduct a theoretical investigation on the Au/Si system. The main objective of this project is to study the behavior of Au atoms deposited onto a Si(100) substrate and measure the surface stress of the system using the MEAM.

1.2 Background

The MEAM is a semi-empirical model based on the embedded atom method (EAM). Compared with *ab initio* calculations, it is less computationally demanding, thus more feasible for calculating large scale structures in which *ab intio* calculations are limited. The EAM was first proposed by Daw and Baskes, based on density functional theory in 1983 to study the hydrogen embrittlement in metals [18]. In 1984, the Rose equation was derived as the universal equation to express pair potentials in the EAM [19]. In 1987, Baskes modified the EAM to include directional bonding and applied it to silicon. In 1989, the silicon EAM model was extended to the silicon-germanium system and was renamed the MEAM [20]. In 1992, the original MEAM was applied to 26 elements: ten fcc, ten bcc, three diamond cubic, and three gaseous materials [21]. In 1994, MEAM was improved for HCP crystal structure [22]. The accuracy of different MEAM calculations has been examined by many different studies [23-28]. In these studies, the lattice constants, elastic constants, cohesive energy, vacancy formation energy, and the structural energy difference were calculated and found to agree quite well with experimental results.

More recently, an MEAM investigation of the Au/Si interface was performed by C. L. Kuo and P. Clancy at Cornell University [29]. Their simulation was concerned with

three issues: critical coverage of Au atoms for Au/Si intermixing, Au concentration in the intermixed region and the influence of temperature on the Au/Si interaction. To our knowledge, this is the first theoretical investigation on these controversial issues and provides a basis for comparison for our simulations on the Au/Si system.

1.3 Scope of this Thesis

This M.Sc.thesis is a continuation of work started during the summer 2005 by undergraduate student John Braeckmann during an NSERC USRA position in our research group. In that time, John wrote an MEAM program and applied it to the Si(100) reconstruction and deposition of 10 Au atoms on a Si(100) surface. The purpose of this thesis is to improve the program originally written by John Braeckmann and to extend its application to study different situations in depositing Au onto the Si(100) surface.

In Chapter 2, the theoretical foundation for the MEAM is given. Chapter 3 outlines the computational details and steps used for validating the code used in our simulations. Chapter 4 discusses the results from our simulations, including the Si(100) reconstruction and the adsorption of Au atoms on the Si(100) surface. Finally, the conclusions obtained from this study will be presented in Chapter 5.

Chapter 2

Theory

In this Chapter, the first section discusses the formalism of the Modified Embedded Atom Method. Following this, the two computational methods used in this work, conjugate gradient minimization and molecular dynamics are described. The last section discusses the surface stress tensor.

2.1 Modified Embedded Atom Method (MEAM)

MEAM is based on a quasiatom theory in which the system is modelled as ions embedded within an electron gas [30]. The ion and its electronic screening cloud constitute a unit called a quasiatom. In the MEAM formalism, the energy of each quasiatom is given by the expression:

$$E_i = F_i(\rho_i) + \frac{1}{2}\sum_{j\neq i}^{N} \varphi_{ij}(r_{ij}) S_{ij} \tag{2.1}$$

where the embedding energy F_i is calculated as a function of the background electron density ρ_i, φ_{ij} is the pair interaction energy and r_{ij} is the distance between atoms i

and j. S_{ij} is the many body screening function which will be defined in 2.1.3. N is the number of atoms in the system.

The total energy of a system containing N atoms is the sum of the individual atomic energies:

$$E_{tot} = \sum_{i=1}^{N} E_i. \tag{2.2}$$

In order to calculate the total energy of the system, functional forms for F_i, ρ_i and φ_{ij} must be determined.

2.1.1 The Embedding Function

The idea of the embedding energy originates from quasiatom theory based on density functional theory. The embedding energy F_i is the energy needed to embed an atom into the background electron density at site i. According to first principles calculations, some important information about the the general behaviors of the embedding function is known: it should go to zero at zero electron density and have a negative slop and positive curvature for the background electon density in metal[31, 32, 33]. Then by fitting the function with elastic constants, lattice constants, sublimation energy and vacancy formation energy, the expression for the embedding energy can be empirically determined as:

$$F_i(\rho_i) = A_i E_i^c \frac{\rho_i}{Z_i} \ln\left(\frac{\rho_i}{Z_i}\right) \tag{2.3}$$

where E_i^c is the cohesive energy of atom i, Z_i is the number of nearest-neighbors of atom i and A_i is a parameter to be fitted (see Section 2.1.5 for details). It has been shown that Equation 2.3 can give the correct relationship between the bond length and the number of bonds [20].

2.1.2 The Background Electron Density

The Embedded Atom Method (EAM) expresses the background electron density at atom i as a sum of the individual atomic electron densities of all other atoms. While this works well for metallic systems, its applicability is limited to systems where forces do not require a non-radial dependence. Thus, EAM cannot model covalent systems. To remedy this, MEAM was developed [34] whereby the background electron density contains three angular terms in addition to the familiar radial term of the EAM. Therefore the MEAM electron density takes the following form where each term is given an appropriate weight t_i:

$$\rho_i = \frac{1}{\rho_i^e}\left[\sum_{l=0}^{3} t_i^{(l)}\left(\bar{\rho}_i^{(l)}\right)^2\right]^{\frac{1}{2}} \tag{2.4}$$

where

$$\bar{\rho}_i^{(0)} = \sum_{j\neq i}^{N} \rho_j^{a(0)}\left(r_{ij}\right) S_{ij} \tag{2.5}$$

$$\left(\bar{\rho}_i^{(1)}\right)^2 = \sum_{\alpha=1}^{3}\left[\sum_{j\neq i}^{N} \frac{r_{ij}^{\alpha}}{r_{ij}} \rho_j^{a(1)}\left(r_{ij}\right) S_{ij}\right]^2 \tag{2.6}$$

$$\left(\bar{\rho}_i^{(2)}\right)^2 = \sum_{\alpha,\beta=1}^{3}\left[\sum_{j\neq i}^{N} \frac{r_{ij}^{\alpha} r_{ij}^{\beta}}{r_{ij}^2} \rho_j^{a(2)}\left(r_{ij}\right) S_{ij}\right]^2 - \frac{1}{3}\left[\sum_{j\neq i}^{N} \rho_j^{a(2)}\left(r_{ij}\right) S_{ij}\right]^2 \tag{2.7}$$

$$\left(\bar{\rho}_i^{(3)}\right)^2 = \sum_{\alpha,\beta,\gamma=1}^{3}\left[\sum_{j\neq i}^{N} \frac{r_{ij}^{\alpha} r_{ij}^{\beta} r_{ij}^{\gamma}}{r_{ij}^3} \rho_j^{a(3)}\left(r_{ij}\right) S_{ij}\right]^2 . \tag{2.8}$$

In Equations 2.5 to 2.8, α, β and $\gamma = 1, 2, 3$ correspond to the x, y, and z directions respectively, such that r_{ij}^{α} is the x, y or z component of the vector $\vec{r}_{ij}$. Each $\rho_j^{a(l)}\left(r_{ij}\right)$ represents the atomic electron density of atom j at a distance r_{ij} from i and takes the form of an exponential decay:

$$\rho_j^{a(l)}(r_{ij}) = \rho_j^e \exp\left[-\beta_j^{(l)}\left(\frac{r_{ij}}{r_j^e} - 1\right)\right] \tag{2.9}$$

where r_j^e is the equilibrium nearest-neighbor separation for atom j. In Equation 2.9, ρ_j^e and $\beta_j^{(l)}$ are parameters representing the electron density scaling factor and the rate of electron density decay respectively. Determination of the parameters t_i, ρ_j^e and $\beta_j^{(l)}$ will be discussed in detail in 2.1.5.

2.1.3 The Many Body Screening Function

In the MEAM, a many body screening function S_{ij} was introduced by Baskes [21] to limit the range of interactions of the atoms. S_{ij} defines the screening between atoms i and j due to the presence of other atoms in the system so that the interaction between atoms that are not nearest neighbors are reduced. In this scheme, the atomic electron densities and the pair potential are multiplied by S_{ij}; thus, if the atoms are unscreened, $S_{ij} = 1$, and if they are completely screened, $S_{ij} = 0$. S_{ij} depends on all of the other atoms in the system and is written as a product of partial screening functions S_{ijk}:

$$S_{ij} = \Pi_{k \neq i,j}^N S_{ijk}. \tag{2.10}$$

Different models have been used to find a functional expression for S_{ijk}. The original model used a form containing a singular point and thus induced difficulties in minimization and molecular dynamics calculations. As a consequence, a new simpler screening function was developed by Baskes *et al.* [35] and was used in this study. In this model, to define the range of screening, S_{ijk} is calculated by considering an ellipse passing through atoms i, j and k as shown in Figure 2.1 where the minor axis is determined by atoms i and j. Atoms outside the dashed curve do not screen atoms

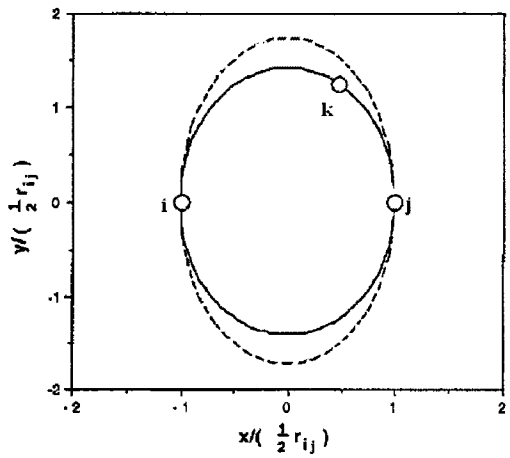

Figure 2.1: Screening of atoms i and j by neighboring atom k [35].

i and j while atoms inside the solid curve screen atoms i and j completely. Therefore, to calculate S_{ijk} the equation of the ellipse should be determined, which is given by

$$x^2 + \frac{y^2}{C} = (\frac{r_{ij}}{2})^2 \tag{2.11}$$

where the parameter C is determined by

$$C = 1 + 2\frac{r_{ij}^2\left(r_{jk}^2 + r_{ik}^2 - r_{ij}^2\right)}{r_{ij}^4 - \left(r_{ik}^2 - r_{jk}^2\right)^2}. \tag{2.12}$$

Then the partial screening function is given by

$$S_{ijk} = \begin{cases} 0 & \text{if } X < 0 \\ \left[1 - (1-X)^4\right]^2 & \text{if } 0 \leq X \leq 1 \\ 1 & \text{if } X > 1 \end{cases} \tag{2.13}$$

where $X = \left(\frac{C - C_{min}}{C_{max} - C_{min}}\right)$. In Figure 2.1, C_{max} corresponds to the dashed ellipse and

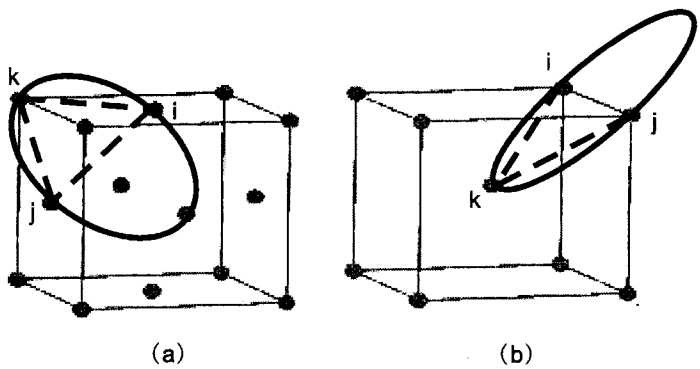

Figure 2.2: Screening of atoms i and j by neighboring atom k in (a) fcc and (b) bcc crystal lattice.

C_{min} corresponds to the solid ellipse. In this study and in most MEAM simulations, $C_{max} = 2.8$ and $C_{min} = 2.0$, which are determined according to the crystal structure of the system. These values are chosen so that the interactions are limited within the first nearest neighbors [35].

To see how the ellipse in Figure 2.1 can be related to the screening function in Equation 2.13, two cases can be considered to facilitate understanding: in the FCC structure, if atom i, j and k are the three nearest neighbors (Figure 2.2 (a)), no atoms are screened because i, j and k are all first nearest neighbors with each other, thus $S_{ijk} = 1$. As in this case, atom k is equidistant from atoms i and j and they form an equilateral triangle, we have $C = 3 \geq 2.8$, which yields $S_{ijk} = 1$ according to Equation 2.13. In the BCC structure, if atoms i and j are the second nearest neighbors and atom k is the first nearest neighbor to i and j (Figure 2.2 (b)), then atom j is screened from atom i by atom k, thus $S_{ijk} = 0$. As atom i, j and k form a right-angled isoceles triangle, we have $C = 2$ which yields $S_{ijk} = 0$ according to Equation 2.13. Considering these two expamples, it is reasonable that Equation 2.13 may be used as an numerical expression of Figure 2.1 and the screening function.

2.1.4 The Pair-Interaction Function

Equation 2.1 has a pair interaction term φ which should be determined. To obtain the expression for φ, the Rose Equation was derived [19]. This is a universal equation to calculate the energy of an atom in a reference structure as a function of the distance between the atoms. The reference structure is a perfect crystal structure with no defect. If the system is in the reference structure, the energy of atom i can be express as:

$$E_i^u(r) = -E_i^c \left(1 + a^* + \frac{\delta_i a^{*3}}{r}\right) exp\left(-a^*\right) \tag{2.14}$$

$$a^* = \alpha_i \left(\frac{r}{r_i^e} - 1\right) \tag{2.15}$$

$$\alpha_i = \sqrt{\frac{9B_i\Omega_i}{E_i^c}} \tag{2.16}$$

where r is the distance between any two atoms, r_i^e is the nearest neighbor distance in the reference structure. δ_i is determined by adjusting the repulsive and attractive energies in the MEAM potential to fit the Local Density Approximation (LDA) calculations [29]. B_i and Ω_i are the bulk modulus and the atomic volume of atom i, respectively.

When the system contains only one atomic species i, the mathematical expression for φ_{ii} can be derived as described below.

Applying Equation 2.14, Equation 2.1 becomes

$$E_i^u(r_{ij}) = F_i\left(\rho_i^{ref}\left(r_{ij}\right)\right) + \frac{1}{2} Z_i \varphi_{ii}\left(r_{ij}\right) \tag{2.17}$$

where, in the reference structure, all the nearest-neighbors of atom i are equidistant

	fcc	bcc	diamond	NaCl
Z_i	12	8	4	6
$s_i^{(1)}$	0	0	0	0
$s_i^{(2)}$	0	0	0	0
$s_i^{(3)}$	0	0	$\frac{32}{9}$	0

Table 2.1: Geometrical factors required for calculating the background electron density in the reference structure.

so that no screening occurs. Rearranging the above equation gives:

$$\varphi_{ii}\left(r_{ij}\right) = \frac{2}{Z_i}\left[E^u\left(r_{ij}\right) - F_i\left(\rho_i^{ref}\left(r_{ij}\right)\right)\right]. \tag{2.18}$$

When dealing with the reference structure, certain geometric relationships exist so that the summations of Equations 2.5 - 2.8 can be replaced with geometrical factors $s_i^{(l)}$ such that

$$\begin{aligned}\rho_i^{ref}\left(r_{ij}\right) &= \frac{1}{\rho_i^e}\sqrt{\sum_{l=0}^{3} t_i^{(l)}(\bar{\rho}_i^{(l)ref})^2} \\ &= \frac{1}{\rho_i^e}\sqrt{\sum_{l=0}^{3} s_i^{(l)} t_i^{(l)}\left[\rho^{a(l)}\left(r_{ij}\right)\right]^2}.\end{aligned} \tag{2.19}$$

As an example, the summation of Equation 2.5 can be replaced with Z_i:

$$\bar{\rho}_i^{(0)^{ref}}\left(r_{ij}\right) = Z_i \rho_i^{a(0)}\left(r_{ij}\right). \tag{2.20}$$

Then we have $s_i^{(0)} = Z_i^2$. $s_i^{(l)}$ for $l = 1-3$ depends on the particular crystal structure being used as the reference structure. Table 2.1 provides these factors for the face-centered cubic (fcc), body-centered cubic (bcc), diamond and B1 (NaCl) structures. Putting these factors according to the corresponding structure into Equation 2.18, the expression for the pair-interaction function between atoms of the same species

can be largely simplified.

For the case where there are two atomic species, we denote the pair potential function as φ_{ij}. For notational purposes, assume atoms i and j are of different atomic species. Before finding φ_{ij}, an appropriate reference structure must be determined. In most situations, the two atomic species of interest will exist in some thermodynamically stable compound and the crystal structure they form can be used as the reference. When two materials do not form a thermodynamically stable compound (i.e. gold and silicon), first principles calculations can be performed to determine the reference structure. In their work, Kuo and Clancy [29] used the B1 (NaCl) structure as a reference of a Au/Si compound. In this kind of structure, the total energy per atom can be written as:

$$E_i\left(r_{ij}\right) = \frac{1}{2}\left(E_{atomi} + E_{atomj}\right) \tag{2.21}$$

where E_{atomi} and E_{atomj} are the energy for atom i and j. Therefore, the same procedure used to obtain φ_{ii} can now be used for φ_{ij} where the reference structure has Z_{ij} nearest-neighbors:

$$E_i^u\left(r_{ij}\right) = \frac{1}{2}\left[F_i\left(\frac{\rho_i^{ref}\left(r_{ij}\right)}{Z_i}\right) + F_j\left(\frac{\rho_j^{ref}\left(r_{ij}\right)}{Z_j}\right) + Z_{ij}\varphi_{ij}\left(r_{ij}\right)\right]. \tag{2.22}$$

Rearranging the above equation gives:

$$\varphi_{ij}\left(r_{ij}\right) = \frac{1}{Z_{ij}}\left[2E_i^u\left(r_{ij}\right) - F_i\left(\frac{\rho_i^{ref}\left(r_{ij}\right)}{Z_i}\right) - F_j\left(\frac{\rho_j^{ref}\left(r_{ij}\right)}{Z_j}\right)\right]. \tag{2.23}$$

In the NaCl structure, each atom i has Z_{ij} nearest-neighbors of type j. Therefore,

$$\bar{\rho}_i^{(0)^{ref}}\left(r_{ij}\right) = Z_{ij}\rho_j^{a(0)}\left(r_{ij}\right). \tag{2.24}$$

And, for all atoms $\bar{\rho}_i^{(1)ref} = \bar{\rho}_i^{(2)ref} = \bar{\rho}_i^{(3)ref} = 0$ (see Table 2.1), so we have :

$$\rho_i^{ref}(r_{ij}) = \frac{Z_{ij}}{\rho_i^e}\rho_j^{a(0)}(r_{ij}). \tag{2.25}$$

Submitting Equation 2.25 into Equation 2.23 gives

$$\varphi_{ij}(r_{ij}) = \frac{1}{Z_{ij}}\left[2E_i^u(r_{ij}) - F_i\left(\frac{Z_{ij}}{Z_i}\frac{\rho_j^{a(0)}(r_{ij})}{\rho_i^e}\right) - F_j\left(\frac{Z_{ij}}{Z_j}\frac{\rho_i^{a(0)}(r_{ij})}{\rho_j^e}\right)\right]. \tag{2.26}$$

2.1.5 Determination of the MEAM Parameters

In the MEAM equations, there are several parameters to be determined from bulk properties, such as A_i in Equation 2.3, t_i in Equations 2.5 to 2.8 and $\beta_j^{(l)}$ in Equation 2.9. A_i can be determined by fitting the fcc-bcc energy difference derived experimentally from phase diagrams or theoretically from first principles calculations. In Yuan *et al.*'s work, the following equation was used to calculate A_i for Li [25]:

$$0.608A_i = 0.5 + \frac{\Delta E_{b-f}}{E_i^c} \tag{2.27}$$

where E_{b-f} is the structure energy difference between fcc and bcc and E_i^c is the cohesive energy.

The electron density weights t_i and exponential decay factors $\beta_j^{(l)}$ are related to elastic constants of the reference structure [21]. As Baskes explained in Ref. [21], in general, the values of $\beta_i^{(1)}$ were not well determined because they were highly correlated and were chosen somewhat arbitrarily; however, small variations in the chosen values did not seem to be particularly important in the calculations of bulk properties such as the surface energy and structural energy of the system.

Another parameter that may be required is the electron density scaling factor ρ_i^e. It can be seen from Equations 2.4 - 2.9 that ρ_j^e appears in the numerator and ρ_i^e appears in the denominator in the expression of the background electron density. Therefore, if a system is comprised solely of one species of atoms, ρ_i^e divides out and becomes irrelevant, thus is often set equal as 1; if not, it can be obtained by fitting the vacancy formation energy. In Kuo and Clancy's work [29], it was shown that the vacancy formation energy could be given by

$$E_v^f = Z_i \left(E_i^{(2)} - E_i^{(1)} \right) \tag{2.28}$$

which contained the electron density scaling factors ρ_i^e implicitly. In Equation 2.28, $E_i^{(1)}$ is the energy per atom for a perfect crystal and $E_i^{(2)}$ is the energy for the neighboring atom, and they always correspond to atoms of different species.

The necessary fitting parameters in MEAM equations were calculated by Baskes [21] for ten fcc, ten bcc and three diamond materials (refer to Table 2.2). Kuo and Clancy [29] calculated a second set of parameters for Au and Si and also provided those needed to describe Au/Si interactions (refer to Table 2.3). In their study, the B1(Nacl) structure was taken as the reference for the Au/Si system because no thermodynamically stable Au/Si compound has been found in nature. Since all the fitting procedures were based on this assumption, the reliability of these parameters can be questioned. In this study, we used parameters calculated by Kuo and Clancy for the Au/Si(100) system. Looking for better parameters is part of our future work.

Table 2.2: MEAM fitting parameters as calculated by Baskes [21]

	E_i^c	r_i^e	α_i	A_i	$\beta_i^{(0)}$	$\beta_i^{(1)}$	$\beta_i^{(2)}$	$\beta_i^{(3)}$	$t_i^{(0)}$	$t_i^{(1)}$	$t_i^{(2)}$	$t_i^{(3)}$
Cu	3.540	2.56	5.11	1.07	3.63	2.2	6.0	2.2	1	3.14	2.49	2.95
Ag	2.850	2.88	5.89	1.06	4.46	2.2	6.0	2.2	1	5.54	2.45	1.29
Au	3.930	2.88	6.34	1.04	5.45	2.2	6.0	2.2	1	1.59	1.51	2.61
Ni	4.450	2.49	4.99	1.10	2.45	2.2	6.0	2.2	1	3.57	1.60	3.70
Pd	3.910	2.75	6.43	1.01	5.31	2.2	6.0	2.2	1	2.34	1.38	4.48
Pt	5.770	2.77	6.44	1.04	4.67	2.2	6.0	2.2	1	2.73	-1.38	3.29
Al	3.580	2.86	4.61	1.07	2.21	2.2	6.0	2.2	1	-1.78	-2.21	8.01
Pb	2.040	3.50	6.06	1.01	5.31	2.2	6.0	2.2	1	2.74	3.06	1.20
Rh	5.750	2.69	6.00	1.05	1.13	1.0	2.0	1.0	1	2.99	4.61	4.80
Ir	6.930	2.72	6.52	1.05	1.13	1.0	2.0	1.0	1	1.50	8.10	4.80
Li	1.650	3.04	2.97	0.87	1.43	1.0	1.0	1.0	1	0.26	0.44	-0.20
Na	1.130	3.72	3.64	0.90	2.31	1.0	1.0	1.0	1	3.55	0.69	-0.20
K	0.941	4.63	3.90	0.92	2.69	1.0	1.0	1.0	1	5.10	0.69	-0.20
V	5.300	2.63	4.83	1.00	4.11	1.0	1.0	1.0	1	4.20	4.10	-1.00
Nb	7.470	2.86	4.79	1.00	4.37	1.0	1.0	1.0	1	3.76	3.83	-1.00
Ta	8.089	2.86	4.90	0.99	3.71	1.0	1.0	1.0	1	4.69	3.35	-1.50
Cr	4.100	2.50	5.12	0.94	3.22	1.0	1.0	1.0	1	-0.21	12.26	-1.90
Mo	6.810	2.73	5.85	0.99	4.48	1.0	1.0	1.0	1	3.48	9.49	-2.90
W	8.660	2.74	5.63	0.98	3.98	1.0	1.0	1.0	1	3.16	8.25	-2.70
Fe	4.290	2.48	5.07	0.89	2.94	1.0	1.0	1.0	1	3.94	4.12	-1.50
C	7.370	1.54	4.31	1.80	5.50	4.3	3.1	6.0	1	5.57	1.94	-0.77
Si	4.630	2.35	4.87	1.00	4.40	5.5	5.5	5.5	1	3.13	4.47	-1.80
Ge	3.850	2.45	4.98	1.00	4.55	5.5	5.5	5.5	1	4.02	5.23	-1.60

Note: In Baskes MEAM $\delta_i = 0$

	Au	Si	Au/Si
A_i	1.04	1.00	
α	6.34	4.87	3.76
$\beta_i^{(0)}$	5.45	4.4	
$\beta_i^{(1)}$	1.2	5.5	
$\beta_i^{(2)}$	6.0	5.5	
$\beta_i^{(3)}$	1.2	5.5	
δ	0.066	0.000	1.270
E^c	3.93	4.63	4.93
r^e	2.88	2.35	2.58
ρ_i^e	0.87	2.05	
$t_i^{(0)}$	1	1	
$t_i^{(1)}$	2.59	2.05	
$t_i^{(2)}$	-1.00	4.47	
$t_i^{(3)}$	4.51	-1.80	

Table 2.3: MEAM fitting parameters as calculated by Kuo and Clancy [29]

2.2 Conjugate Gradient Minimization

Conjugate gradient methods can be used in minimizing a multidimensional function. When a one dimensional function $f(x)$ is minimized, we need to test the variable x with different values to find the minimum. Since all these different values of x are in the same direction, a one dimensional minimization is called a *line minimization*. When an N-dimensional function $f(\mathbf{x})$ is minimized, if we start at a point $\mathbf{x}_0$ and proceed in a direction $\mathbf{n}$ to test different variables, then $f(\mathbf{x})$ can be minimized locally from $\mathbf{x}_0$ to $\mathbf{x}_0 + \mathbf{n}$ like the one dimensional minimization. Thus, we can break the N-dimensional minimization into many small line minimizations along different directions so that variables along the N directions can be tested to find the global minimum of $f(\mathbf{x})$. To fulfill this, the function should proceed to another point $\mathbf{v}$ to perform another line minimization once a local minimization from $\mathbf{x}_0$ to $\mathbf{x}_0 + \mathbf{n}$ is finished. Determination of the direction of $\mathbf{v}$ is the main task in multidimensional

minimization. It is very important due to its influence on the accuracy and efficiency of the minimization.

Conjugate gradient minimization distinguishes from other minimization methods in its way of choosing the direction of $\mathbf{n}$ and $\mathbf{v}$. It is known that once $f(\mathbf{x})$ is minimized within $\mathbf{x}_0$ and $\mathbf{x}_0 + \mathbf{n}$, the gradient of the function must be perpendicular to $\mathbf{n}$ at the line minimum. Then the condition that the motion along $\mathbf{v}$ does not ruin the minimization along $\mathbf{n}$ is that the gradient stays perpendicular to $\mathbf{n}$. This principle can be seen more explicitly in a simpler case: if the 3-dimensional function $f(x, y, z)$ has been minimized from 0 to x_0 at x_{min} along x direction, we have

$$\begin{aligned} \nabla f(x,y,z)\Big|_{(x_{min},0,0)} \cdot \hat{x} &= \left(\frac{\partial f}{\partial x}\hat{x} + \frac{\partial f}{\partial y}\hat{y} + \frac{\partial f}{\partial z}\hat{z}\right)\Big|_{(x_{min},0,0)} \cdot \hat{x} \\ &= \frac{\partial f}{\partial x}\Big|_{(x_{min},0,0)} = 0 \end{aligned} \tag{2.29}$$

where $f(x, y, z)$ is the gradient of $f(x, y, z)$, $\hat{x}$, $\hat{y}$ and $\hat{z}$ are unit vectors in the x, y and z directions. Equation 2.29 shows when $f(x, y, z)$ is minimized at $(x_{min}, 0, 0)$ from 0 to x_0, its gradient at $(x_{min}, 0, 0)$ is perpendicular to $\hat{x}$. Then when we want to minimize $f(x, y, z)$ in another direction so that it is minimized globally, the most efficient way is to move in the $x = x_{min}$ plane, in which any gradient of $f(x_{min}, y, z)$ is still perpendicular to the x direction. Proceeding in other directions out of the $x = x_{min}$ plane will increase the value of the function in the x direction, thus ruining the minimization along the x direction.

Therefore, we need a numerical expression to describe the condition that the gradient of $f(\mathbf{x})$ stays perpendicular to $\mathbf{n}$ while moving along $\mathbf{v}$. If we take a particular point $\mathbf{x}'$ as the origin of the coordinate system with the coordinates $\mathbf{x}$, then $f(\mathbf{x})$ can

be approximated by its Taylor series:

$$f(\mathbf{x}) = f\left(\mathbf{x}'\right) + \sum_i \frac{\partial f}{\partial x_i} x_j + \frac{1}{2} \sum_{i,j} \frac{\partial^2 f}{\partial x_i \partial x_j} x_i x_j + \ldots \simeq \mathbf{c} - b \cdot \mathbf{x} + \frac{1}{2} \mathbf{x} \cdot \mathbf{A} \cdot \mathbf{x}. \quad (2.30)$$

where $\mathbf{c} \equiv f\left(\mathbf{x}'\right), \mathbf{b} \equiv -\nabla f\Big|_{\mathbf{x}'}, [\mathbf{A}]_{ij} \equiv \frac{\partial f}{\partial x_i} x_j\Big|_{\mathbf{x}'}$.

According to Equation 2.30, the gradient of f can be calculated as

$$\nabla f = \mathbf{A} \cdot \mathbf{x} - \mathbf{b}. \quad (2.31)$$

When the function is calculated along some direction, the change of ∇f is

$$\delta(\nabla f) = \mathbf{A} \cdot (\delta(\mathbf{x})). \quad (2.32)$$

The condition that the gradient of $f(\mathbf{x})$ stays perpendicular to $\mathbf{n}$ while moving along $\mathbf{v}$ requires that

$$0 = \mathbf{n} \cdot \delta(\nabla f) = \mathbf{n} \cdot \mathbf{A} \cdot \mathbf{v}. \quad (2.33)$$

As $\mathbf{n}$ is known and $\mathbf{A}$ is determined by Equation 2.30, $\mathbf{v}$ can be calculated according to Equation 2.33. When Equation 2.33 holds for two vectors $\mathbf{n}$ and $\mathbf{v}$, they are said to be conjugate with each other [36]. If the successive line minimizations are done along the conjugate set of directions, it continually refines the direction toward the minimum without ruining the previous minimization; thus, it requires a smaller number of the iterations in the program and provides more efficient convergence to minimum.

2.3 Molecular Dynamics (MD)

Because conjugate gradient minimization does not consider thermal motion, it is useful for finding the 0 K equilibrium of a system. The equilibrium configurations

at non-zero temperature can be determined using molecular dynamics, which can be combined with MEAM (MEAM-MD) to solve dynamic problems such as simulations of reaction processes. Molecular dynamics (MD) is an iterative process perfectly suited for today's computers. Its strength lies in its ability to follow time dependent trajectories of a many particle system using Newtonian mechanics, which is what a Monte Carlo (MC) simulation fails to do. Hence, MD is capable of moving a system with a particular set of initial conditions towards equilibrium.

2.3.1 The Verlet Velocity Algorithm

Before MD begins, expressions for energy, force, velocity and position must be known. In this study, the force acting on the i^{th} atom is given by (refer to 3.2.3 for derivation):

$$m_i \cdot \vec{a}_i = -\left\{ \sum_{j=1}^{N} F_j^{'}(\rho_j)\, \vec{\nabla}_i \rho_j + \sum_{j \neq i}^{N} S_{ij} \varphi_{ij}^{'}(r_{ij}) \frac{\vec{r}_{ij}}{r_{ij}} + \frac{1}{2} \sum_{j=1}^{N} \sum_{k \neq j}^{N} \varphi_{jk}(r_{jk})\, \vec{\nabla}_i S_{jk} \right\} \tag{2.34}$$

where the force is denoted by mass multiplied by acceleration to avoid confusion with the embedding function $F_i(\rho_i)$ shown in Equation 2.3.

The initial position $\vec{r}_0$ and initial velocity $\vec{v}_0$ are given as the input before the simulations. Given these initial conditions, the velocity $\vec{v}_i$ and position $\vec{r}_i$ can be obtained by numerically integrating the acceleration. In this study, we use the verlet velocity algorithm, which is shown schematically in Figure 2.3, as the technique for the numerical integration. The verlet velocity algorithm was chosen not only for its simplicity but also because it is based on a second order Taylor expansion which minimizes round-off errors. In the verlet velocity algorithm, the velocity of the i^{th} atom at the $(n+1)^{th}$ iteration is written as

$$\vec{v}_{i,n+1} = \vec{v}_{i,n} + \frac{1}{2}\left(\vec{a}_{i,n+1} + \vec{a}_{i,n}\right)\Delta t \tag{2.35}$$

and the position of the i^{th} atom at the $(n+1)^{th}$ iteration as

$$\vec{r}_{i,n+1} = \vec{r}_{i,n} + \vec{v}_{i,n}\Delta t + \frac{1}{2}\vec{a}_{i,n}\left(\Delta t\right)^2. \tag{2.36}$$

Therefore, the verlet velocity algorithm starts with $\vec{r}_{i,n}$ and $\vec{v}_{i,n}$ and calculates $\vec{a}_{i,n}$ in the n^{th} iteration. It provides both the atomic positions and velocities at the same instant of time. Compared with other algorithms such as the original verlet algorithm and predictor-corrector method, it requires less computer memory, because only one set of positions, forces and velocities need to be stored at any one time [37]. This algorithm also conserves energy well even with relatively long time steps.

2.3.2 Temperature Control

An important aspect of molecular dynamics is temperature control. It is useful to attain the desired temperature during equilibration so that the molecular dynamics simulations can be performed at a constant temperature. In this method, the temperature of the system is controlled by adjusting the velocities, which ensures the equipartion of energy is satisfied. The equipartition of energy principle is given by

$$K = \frac{d}{2}Nk_BT \tag{2.37}$$

where K is kinetic energy, d is the number of degrees of freedom per particle, k_B is Boltzmann's constant and T is temperature. For atoms moving in three dimensions $d = 3$. Therefore, T is given by

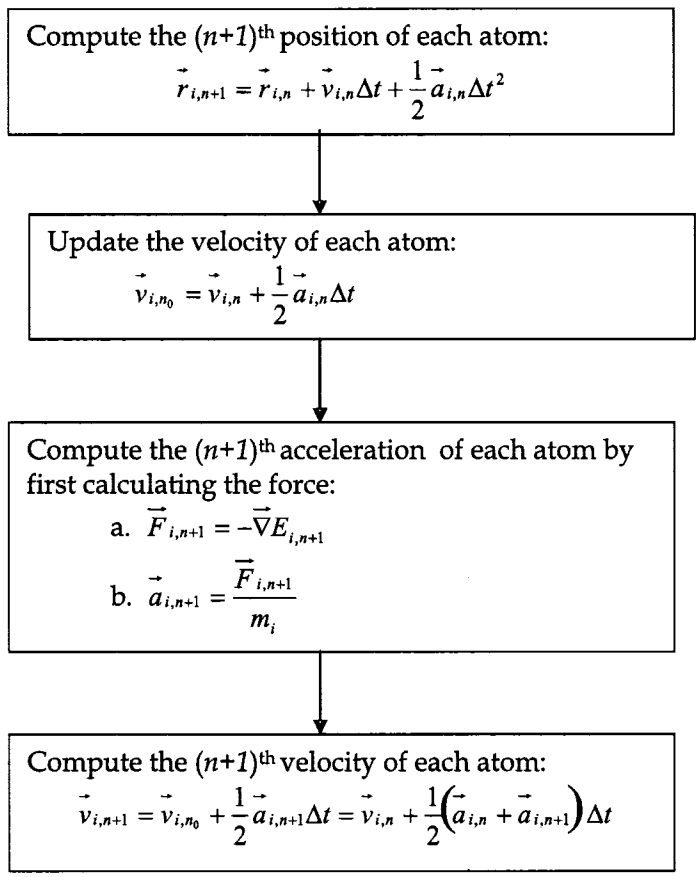

Figure 2.3: Flowchart illustrating one step of the verlet velocity algorithm.

$$T = \frac{m}{3Nk_B}\sum_{i=1}^{N} {v_i}^2. \tag{2.38}$$

Once velocities have been calculated, T is compared to the desired, user-specified temperature T_D. If these two temperatures do not match , the atomic velocities are adjusted using the following relation:

$$\vec{v}_{i,new} = \sqrt{\frac{T_D}{T}}\vec{v}_{i,old}. \tag{2.39}$$

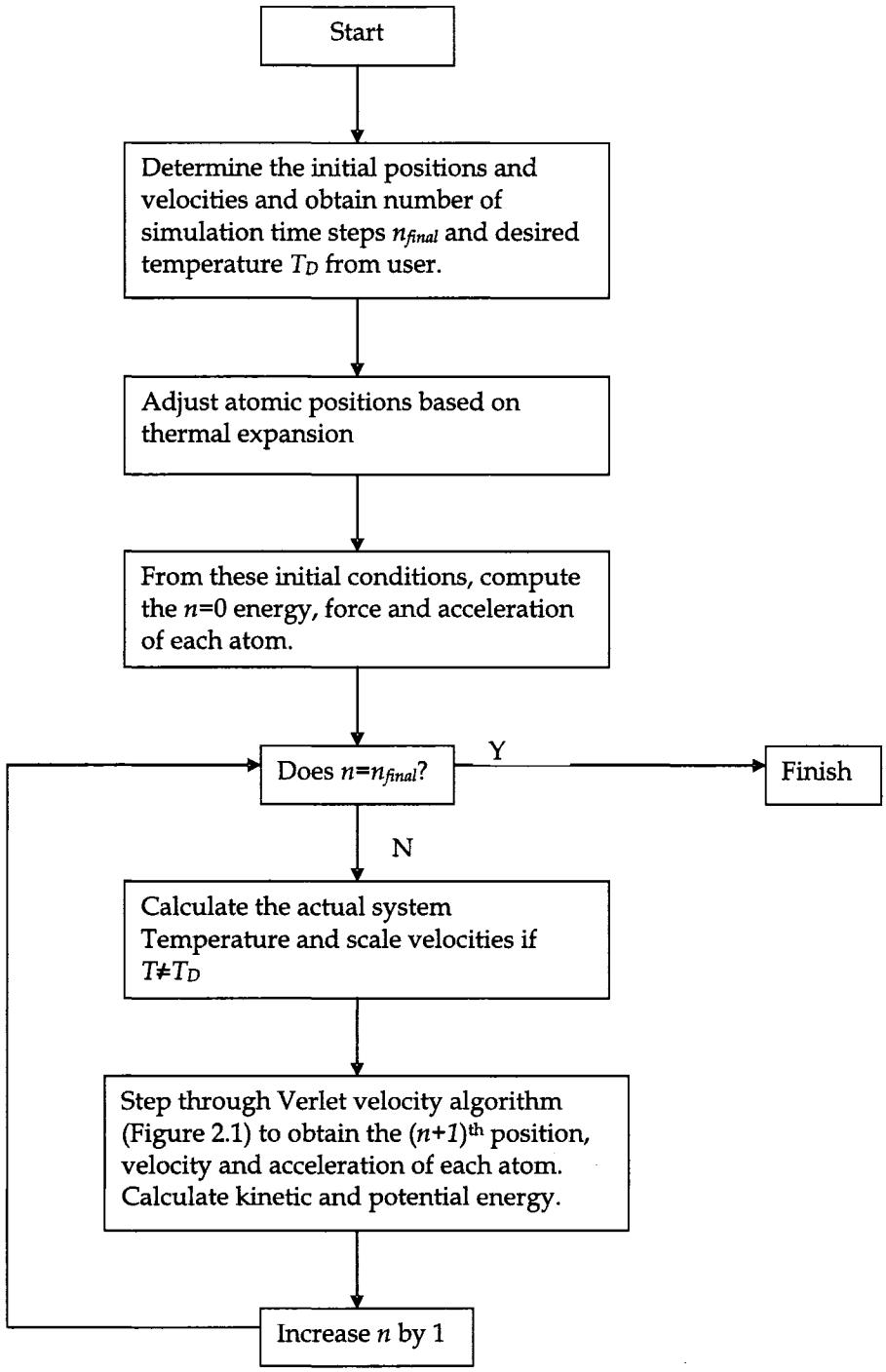

Figure 2.4: Flowchart illustrating molecular dynamics. n is the number of iteration. T is the temperature of the system.

Whenever T and T_D differ, thermal energy (heat) must be added to or removed from the system via Equation 2.39. Energy stability occurs once the system reaches a state of thermal equilibrium $T = T_D$, at which point heat is no longer added or removed. Henceforth, equilibrium will represent this state. Above all, Equations (2.1), (2.34), (2.35), (2.36) and (2.39) can be used to completely describe an MEAM-MD simulation. Figure 2.4 provides a flow chart illustrating the process.

2.4 Surface Stress Tensor

Surface energy is defined as the energy required to create a unit area of surface [38]. Creating the surface consumes energy because the bonds between the atoms are destroyed when the bulk is cleaved into two parts; thus, the surface is less energetically favorable and contains more energy than the bulk does. If E_0 and E_f are the energy of the system before and after the surface is created, then we have

$$E_f = 2E_s + E_0 \tag{2.40}$$

where $2E_s$ is the energy difference which is positive. As two surfaces are created when a bulk is cleaved into two parts, E_s is the energy required to create each of these two surfaces. In this study, before the bulk is cleaved to form the surface, the system has a reference structure with all the atoms placed at their equilibrium positions; thus, $E_0 = NE_c$ in which E_c is the cohesive energy and N is the number of the atoms in the system. E_f can be calculated from Equation (2.1). Therefore, we can define the energy to create a surface as

$$E_s = \frac{1}{2}\left[\sum_{i=1}^{N} E_i - NE_c\right]. \tag{2.41}$$

If A_s is the area of each surface, the surface energy can then be expressed as

$$\sigma = \frac{1}{2A_s}\left[\sum_{i=1}^{N} E_i - NE_c\right]. \tag{2.42}$$

Since the cohesive energy E_c depends on temperature, the surface energies calculated under different conditionals are comparable only at the same temperature.

Suppose now that the surface area changes due to some internal or external force. It can be assumed that the changes in energy caused by these forces are described by linear elasticity theory. The variable used to quantify these effects is the surface stress tensor $\overleftrightarrow{\tau}$. Elements of the surface stress tensor $\tau_{\alpha\beta}$ are given by [39]:

$$\tau_{\alpha\beta} = \frac{1}{A_s}\frac{\partial(\sigma A_s)}{\partial \epsilon_{\alpha\beta}} \tag{2.43}$$

where $\epsilon_{\alpha\beta}$ is an element of the strain tensor. A negative $\tau_{\alpha\beta}$ tends to increase the surface area whereas a positive $\tau_{\alpha\beta}$ tends to decrease it.

The physical interpretation of the nine components of $\overleftrightarrow{\tau}$ is as follows. First, consider an imaginary cube surrounding the surface. Along each face of this cube are three stress components: one direct stress and two shear stresses. A direct stress tends to change the volume of the cube (i.e. expansion or compression) while a shear stress tries to alter the shape of the cube whilst keeping the volume unchanged. Because the system is in static equilibrium, only three of these faces and their stresses need to be considered. Hence, a second rank tensor with nine components is required to describe all of the stresses:

$$\overleftrightarrow{\tau} = \begin{pmatrix} \tau_{xx} & \tau_{xy} & \tau_{xz} \\ \tau_{yx} & \tau_{yy} & \tau_{yz} \\ \tau_{zx} & \tau_{zy} & \tau_{zz} \end{pmatrix}. \tag{2.44}$$

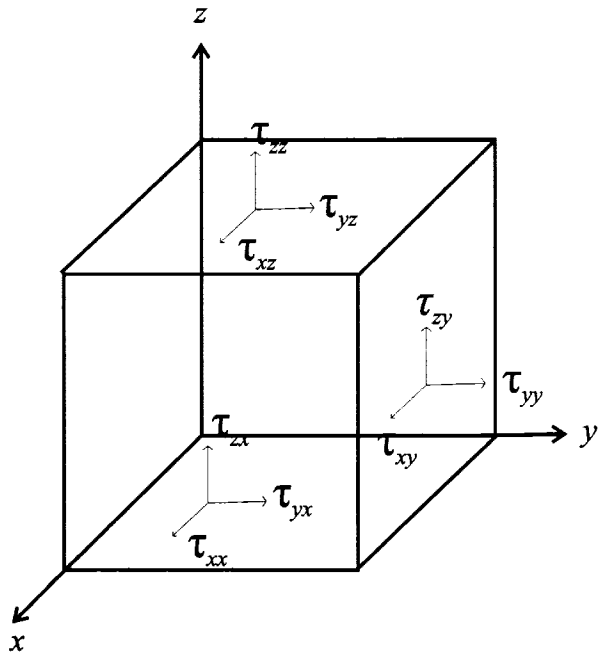

Figure 2.5: A visualization of the nine components of the surface stress tensor.

These nine components, however, are reduced to six unique components because static equilibrium requires $\tau_{xy} = \tau_{yx}$, $\tau_{xz} = \tau_{zx}$ and $\tau_{yz} = \tau_{zy}$. For example, if $\tau_{xy} \neq \tau_{yx}$, a moment would exist and the cube could rotate about the z-axis. In the subscript notation, α is the direction of the stress and β is the direction of the normal of the plane upon which the stress acts. Figure 2.5 gives a diagrammatical representation of $\overleftrightarrow{\tau}$. Combining Equation 2.43 and Equation 2.42, we have:

$$\begin{aligned} \tau_{\alpha\beta} &= \frac{1}{A_s}\frac{\partial}{\partial\epsilon_{\alpha\beta}}\left[\sum_{i=1}^{N} E_i - NE_c\right] \\ &= \frac{1}{A_s}\frac{\partial}{\partial\epsilon_{\alpha\beta}}\sum_{i=1}^{N} E_i. \end{aligned} \tag{2.45}$$

It has been shown [40] that Equation (2.45) can be expressed as a derivative with respect to interatomic distances rather than a derivative with respect to a strain:

$$\tau_{\alpha\beta} = -\frac{1}{A_s}\sum_i \sum_{k\neq i} r_{ik}^{\beta}\frac{\partial E_i}{\partial r_k^{\alpha}}. \tag{2.46}$$

Now substituting Equation 2.1 into Equation 2.46, we have:

$$\begin{aligned}
\tau_{\alpha\beta} &= -\frac{1}{A_s}\sum_i \sum_{k\neq i} r_{ik}^{\beta}\frac{\partial}{\partial r_k^{\alpha}}\left[F_i(\rho_i) + \frac{1}{2}\sum_{j\neq i}\varphi_{ij}(r_{ij})S_{ij}\right] \\
&= -\frac{1}{A_s}\sum_i \sum_{k\neq i} r_{ik}^{\beta}\left[F_i'(\rho_i)\frac{\partial \rho_i}{\partial r_k^{\alpha}} + \frac{1}{2}\sum_i \varphi_{ij}'(r_{ij})\frac{\partial r_{ij}}{\partial r_k^{\alpha}}S_{ij} + \frac{1}{2}\sum_{j\neq i}\varphi_{ij}(r_{ij})\frac{\partial S_{ij}}{\partial r_k^{\alpha}}\right] \\
&= -\frac{1}{A_s}\sum_i \sum_{k\neq i} r_{ik}^{\beta}F_i'(\rho_i)\frac{\partial \rho_i}{\partial r_k^{\alpha}} - \frac{1}{2A_s}\sum_i \sum_{k\neq i} r_{ik}^{\beta}\sum_{j\neq i}\varphi_{ij}'(r_{ij})\frac{r_{ij}^{\alpha}}{r_{ij}}(\delta_{i,k}-\delta_{j,k})S_{ij} \\
&- \frac{1}{2A_s}\sum_i \sum_{k\neq i} r_{ik}^{\beta}\sum_{j\neq i}\varphi_{ij}(r_{ij})\frac{\partial S_{ij}}{\partial r_k^{\alpha}} \\
&= -\frac{1}{A_s}\sum_i \sum_{k\neq i} r_{ik}^{\beta}F_i'(\rho_i)\frac{\partial \rho_i}{\partial r_k^{\alpha}} - \frac{1}{2A_s}\sum_i \sum_{k\neq i} r_{ik}^{\beta}\sum_{j\neq i}\varphi_{ij}'(r_{ij})\frac{r_{ij}^{\alpha}}{r_{ij}}\delta_{i,k}S_{ij} \\
&+ \frac{1}{2A_s}\sum_i \sum_{k\neq i} r_{ik}^{\beta}\sum_{j\neq i}\varphi_{ij}'(r_{ij})\frac{r_{ij}^{\alpha}}{r_{ij}}\delta_{j,k}S_{ij} - \frac{1}{2A_s}\sum_i \sum_{k\neq i} r_{ik}^{\beta}\sum_{j\neq i}\varphi_{ij}(r_{ij})\frac{\partial S_{ij}}{\partial r_k^{\alpha}}.
\end{aligned} \tag{2.47}$$

Because the summation over k in the second term of Equation 2.47 does not include i and the Kronecker delta is non-zero only when $k = i$, this term disappears. Similarly, the Kronecker delta in the third term of Equation 2.47 removes the summation over j, leaving the final expression:

$$\begin{aligned}\tau_{\alpha\beta} &= -\frac{1}{A_s}\sum_i\sum_{j\neq i} r_{ij}^{\beta} F_i^{'}\left(\rho_i\right)\frac{\partial\rho_i}{\partial r_j^{\alpha}} \\ &+ \frac{1}{2A_s}\sum_i\sum_{j\neq i} r_{ij}^{\beta}\varphi_{ij}^{'}\left(r_{ij}\right)\frac{r_{ij}^{\alpha}}{r_{ij}}S_{ij} \\ &- \frac{1}{2A_s}\sum_i\sum_{k\neq i} r_{ik}^{\beta}\sum_{j\neq i}\varphi_{ij}\left(r_{ij}\right)\frac{\partial S_{ij}}{\partial r_k^{\alpha}}.\end{aligned} \tag{2.48}$$

Therefore, using MEAM formalism Equation 2.43 can be calculated.

Chapter 3

MEAM programs

In this chapter, details about the MEAM-MD simulations such as the cut-off distance, periodic boundary conditions and determination of the time step will be discussed. This chapter also includes the steps taken to validate the code by examining the conjugate gradient minimization, calculations of surface energy and the expression of the force in the MEAM program.

3.1 Details about the MEAM-MD Simulations

3.1.1 Cut-off Distance

In the MEAM program, besides the screening function, another scheme used for further limiting the range of interaction is the cut-off distance. By introducing the cut-off distance, interactions between atoms are considered only within a certain distance. Therefore, the calculations are simplified and the computation time can be reduced. The interactions can be ignored beyond the cut-off distance because the potential energy between two atoms and the atomic electron density (Equation 2.9) both approach zero [41]. Figure 3.1 shows that the two body potential and the

atomic electron density of the Si atoms vanish beyond 5.0 Å. Before the program was applied, a suitable radial cut-off distance was determined for a system of 8×8×8 Si atoms. Different values for the cut-off distance were tested in the program and the corresponding total energies were calculated. It was found that when the cutoff distance was greater than 4.23 Å, the calculated total energy stayed constant. This indicated that 4.23 Å was the shortest cut-off distance which ensured all the nonzero interactions were included. Therefore, in this study, the cut-off distance was chosen as 4.23 Å and interactions between atoms were not included beyond this distance.

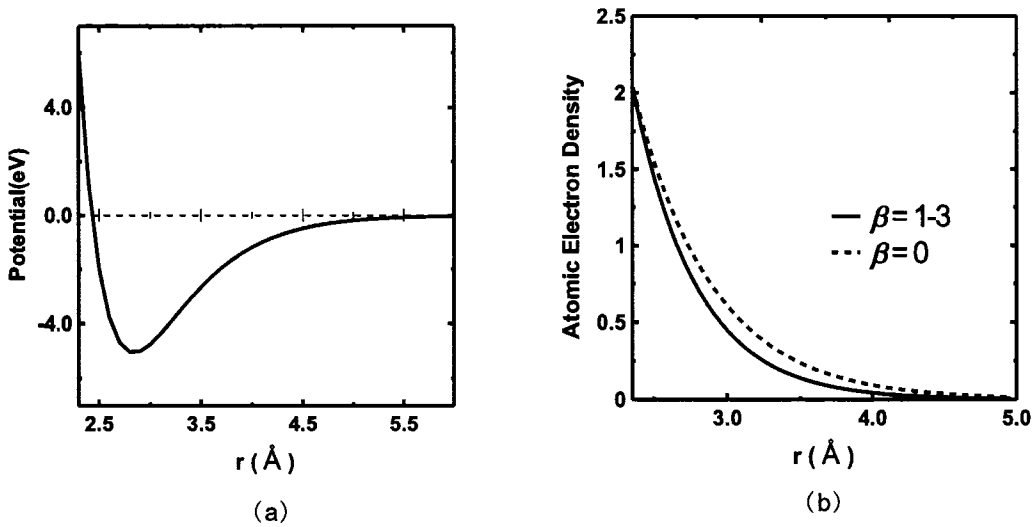

Figure 3.1: (a) Potential energy as a function of separation distance between two Si isolated atoms. (b) Exponential decaying of the atomic electron density of Si atoms.

3.1.2 Period Boundary Conditions

In MEAM-MD simulations, periodic boundary conditions were applied to minimize finite size effects. With periodic boundary conditions, the simulation region is mapped topologically so that there are infinite copies of the boxes in all directions. In Figure 3.2, the central box is surrounded by imaginary neighbors. The coordinates of the

image atoms in the surrounding box are related to those in the center box by simple translations. In this configuration, any atom that leaves the simulation from one side of the box re-enters the simulation region from the other side of the box. For example, suppose the x coordinate is defined to be between $-L_x/2$ and $L_x/2$, where L_x is the width of the box in the x dimension, then if $x \geq L_x/2$, it is replaced by $x - L_x$; if $x \leq -L_x/2$, it is replaced by $x + L_x$. Another consequence is that atoms in the box are able to interact with atoms in the neighboring box near the boundary, which means atom i in the primary box in Figure 3.2 can interact with atom j in box III. If the distance between atom i and j $x_{ij} \geq L_x/2$, it is replaced by $x_{ij} - L_x$; similarly, if $x_{ij} \leq -L_x/2$, it is replaced by $x_{ij} + L_x$.

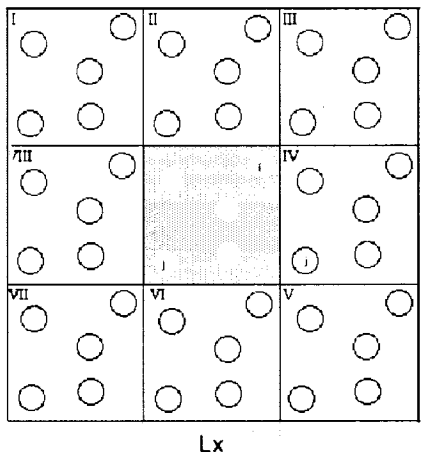

Figure 3.2: Two dimensional box in the periodic boundary conditions.

In MD simulations, if no periodic boundary conditions were applied, the atoms in the finite system would be affected by the boundaries of the system. Therefore, the finite system cannot produce reliable results to study the corresponding infinite system [42]. With periodic boundary conditions, we can use systems containing 500-1000 atoms to simulate infinite systems with the thermostat turned off. In this

study, periodic boundary conditions were applied in the ⟨100⟩ and ⟨010⟩ directions. Because the normal of the Si(100) surface is in the z direction, no periodic boundary condition need be applied in the ⟨001⟩ direction. For our calculations, we chose a two dimensional box with a surface size that contained 8×8 atoms.

3.1.3 Determination of the Time Step

The size of the integration step Δt in Verlet velocity algorithm plays a significant role in the effectiveness of MD routine. If Δt is too small the evolution of the system will be too slow. If on the other hand Δt is too large the numerical integration is inaccurate. Luckily, conservation of energy provides a means of determining Δt: one must ensure the sum of the kinetic and potential energies for the entire system remains constant for an extended period of time [42]. The optimum choice of Δt is the largest possible value allowed before the energy of the system ceases to be stable. In our simulations, this value is found to be $4.125\text{x}10^{-16}$ s. This time step is taken 100,000 times in the simulation; thus, the simulation length is 4.125×10^{-11} s.

3.2 Validating the Code

Once the fundamental MEAM programs had been written, the original author John Braeckman performed initial tests to ensure the accuracy of the calculations, including conjugate gradient minimization, the surface energies and the force expression given by Equation 2.34. The methods used to calculate these quantities are described below.

3.2.1 Test of Conjugate Gradient Minimization

To test the accuracy of conjugate gradient minimization in the MEAM simulations, we used a system of three Si atoms forming an equilateral triangle. Then, the con-

figuration corresponding to the minimum energy was obtained by conjugate gradient minimization. Different initial configurations (not too far away from equilibrium) were tested, and as expected, the final configurations were identical after minimization. In the final configuration, the three Si atoms still formed an equilateral triangle, but the side length was changed. The final side length was 2.5452 Å and the minimized energy was -8.8345 eV.

L	2.0	2.5	3.0	3.5	4.0	4.5	5.0	5.5	6.0
Energy	8.7669	-8.7825	-6.3467	-3.1745	-1.4057	-0.5887	-0.2393	-0.0956	-0.0378
L	2.51	2.52	2.53	2.54	2.55	2.56	2.57	2.58	2.59
Energy	-8.8035	-8.8188	-8.8289	-8.8340	-8.8340	-8.8294	-8.8206	-8.8072	-8.7900
L	2.541	2.542	2.543	2.544	2.545	2.546	2.547	2.548	2.549
Energy	-8.8340	-8.8345	-8.8345	-8.8345	-8.8345	-8.8345	-8.8345	-8.8345	-8.8340

Table 3.1: Total energy of the Si quilateral triangle Maple 7 and a Fortran program with different side lengths L. Values for the energy are given in eV. Values for the side lengths L are given in Å.

To check this result, it is necessary to use a different method to get the equilibrium configuration. We constructed several equilateral triangles with different side lengths and calculated their energy with Maple 7 and a Fortran program. It was found that these two programs gave the same results which might ensure the accuracy of the calculations. We started these calculations from using different side lengths from 2.0 to 6.0 Å which were equally separated by 0.5 Å. The results are shown in the first two rows of Table 3.1. It can be seen that the side length which gave the minimum energy might be around 2.5 Å. Then we set the range of the side lengths from 2.51 to 2.59 Å and found the minimum energy should be given by a side length between 2.54 and 2.55 Å as show in the fourth row of Table 3.1. The last two rows of Table 3.1 show the energy of the Si equilateral triangles with side length from 2.541 to 2.549 Å. It was verified that the minimum energy -8.8345 eV did exist and the corresponding side length could be localized between 2.542 and 2.548 Å, which agreed to the result

obtained from conjugate gradient minimization within 0.2%.

3.2.2 Surface Energy

Calculating the surface energy requires one to first calculate Equation (2.1), the most important equation in the MEAM formalism. Therefore, it is imperative that this equation should be calculated properly.

Using our code with the parameters given in table 2.2, the surface energies of the (100) and (111) faces were calculated for the same ten fcc, ten bcc and three diamond materials used by Baskes [21]. The results of our calculations are given in Table 3.2 and are compared to Table V of [21]. As can be seen, all surface energies agree within 1%. Any discrepancies can be attributed to computational precision.

	(100)	(100)[a]	(111)	(111)[a]		(100)	(100)[a]	(111)	(111)[a]		(100)	(100)[a]	(111)	(111)[a]
Cu	1653	1651	1411	1409	Li	431	431	311	279	C	6242	6195	5121	5082
Ag	1277	1271	1093	1087	Na	288	288	202	202	Si	1883	1878	1256	1253
Au	1085	1084	887	886	K	182	182	125	125	Ge	1660	1658	1156	1154
Ni	2437	2435	2039	2036	V	2499	2490	1811	1805					
Pd	1663	1659	1385	1381	Nb	2791	2788	2027	2018					
Pt	2171	2167	1659	1656	Ta	3299	3292	2310	2305					
Al	902	897	621	618	Cr	1230	1230	1246	1247					
Pb	425	424	367	366	Mo	2124	2122	1862	1861					
Rh	2901	2902	2597	2598	W	2650	2646	2251	2247					
Ir	2900	2907	2828	2835	Fe	2298	2289	1727	1720					

[a] Data from Reference [21]

Table 3.2: Surface energies for various materials and crystal faces using the parameters of Baskes [21]. The results are compared with those calculated by Baskes in [21]. Values are given in erg/cm^2.

3.2.3 Expression of the Force

The expression of the force can be determined by the derivative of equation 2.2. In this study, the force acting on the i^{th} atom is given by:

$$m_i \cdot \vec{a}_i = -\left\{ \sum_{j=1}^{N} F_j'(\rho_j)\, \vec{\nabla}_i \rho_j + \sum_{j \neq i}^{N} S_{ij} \varphi_{ij}'(r_{ij}) \frac{\vec{r}_{ij}}{r_{ij}} + \frac{1}{2} \sum_{j=1}^{N} \sum_{k \neq j}^{N} \varphi_{jk}(r_{jk})\, \vec{\nabla}_i S_{jk} \right\} \quad (3.1)$$

which is derived as described below.

In the MEAM, the potential energy of a system of N atoms is

$$\begin{aligned} E_{tot} &= \sum_{j=1}^{N} E_j \\ &= \sum_{j=1}^{N} F_j\left(\rho_j\right) + \frac{1}{2}\sum_{j=1}^{N}\sum_{k\neq j}^{N} \varphi_{jk}(r_{jk}) S_{jk}. \end{aligned} \tag{3.2}$$

The force acting on atom i is given as

$$\begin{aligned} \frac{\vec{a}_i}{m_i} &= -\vec{\nabla}_i E_{tot} \\ &= -\left(\frac{\partial E_{tot}}{\partial x_i}\hat{x} + \frac{\partial E_{tot}}{\partial y_i}\hat{y} + \frac{\partial E_{tot}}{\partial z_i}\hat{z}\right). \end{aligned} \tag{3.3}$$

Therefore, the main task is to find the expression of $\frac{\partial E_{tot}}{\partial x_i}$ using Equation (3.2):

$$\frac{\partial E_{tot}}{\partial x_i} = \sum_{j=1}^{N} F_j^{'}\left(\rho_j\right)\frac{\partial \rho_j}{\partial x_i} + \frac{1}{2}\sum_{j=1}^{N}\sum_{k\neq j}^{N}\left[S_{jk}\varphi_{jk}^{'}\left(r_{jk}\right)\frac{\partial r_{jk}}{\partial x_i} + \varphi_{jk}\frac{\partial S_{jk}}{\partial x_i}\right]. \tag{3.4}$$

Since $r_{jk} = \sqrt{x_{jk}^2 + y_{jk}^2 + z_{jk}^2}$, $\frac{\partial r_{jk}}{\partial x_i}$ becomes:

$$\begin{aligned} \frac{\partial r_{jk}}{\partial x_i} &= \frac{(x_{jk})}{\sqrt{x_{jk}^2 + y_{jk}^2 + z_{jk}^2}}\left(\frac{\partial x_j}{\partial x_i} - \frac{\partial x_k}{\partial x_i}\right) \\ &= \frac{(x_{jk})}{\sqrt{x_{jk}^2 + y_{jk}^2 + z_{jk}^2}}\left(\delta_{j,i} - \delta_{k,i}\right) \end{aligned} \tag{3.5}$$

where $x_{jk} = x_j - x_k$ and $\delta_{p,q}$ is a Kronecker delta (1 if $p = q$ and 0 if $p \neq q$).

So, putting Equation 3.5 into Equation 3.4 we have

$$\begin{aligned}\frac{\partial E_{tot}}{\partial x_i} &= \sum_{j=1}^{N} F_j^{'}(\rho_j)\frac{\partial \rho_j}{\partial x_i} + \frac{1}{2}\sum_{j=1}^{N}\sum_{k\neq j}^{N} S_{jk}\varphi_{jk}^{'}(r_{jk})\frac{x_{jk}}{r_{jk}}\delta_{j,i} \\ &- \frac{1}{2}\sum_{j=1}^{N}\sum_{k\neq j}^{N} S_{jk}\varphi_{jk}^{'}(r_{jk})\frac{x_{jk}}{r_{jk}}\delta_{k,i} + \frac{1}{2}\sum_{j=1}^{N}\sum_{k\neq j}^{N}\varphi_{jk}(r_{jk})\frac{\partial S_{jk}}{\partial x_i} \\ &= \sum_{j=1}^{N} F_j^{'}(\rho_j)\frac{\partial \rho_j}{\partial x_i} + \frac{1}{2}\sum_{k\neq i}^{N} S_{ik}\varphi_{ik}^{'}(r_{ik})\frac{x_{ik}}{r_{ik}} \\ &- \frac{1}{2}\sum_{j\neq i}^{N} S_{ji}\varphi_{ji}^{'}(r_{ji})\frac{x_{ji}}{r_{ji}} + \frac{1}{2}\sum_{j=1}^{N}\sum_{k\neq j}^{N}\varphi_{jk}(r_{jk})\frac{\partial S_{jk}}{\partial x_i}.\end{aligned} \tag{3.6}$$

But, $r_{ji} = r_{ij}$ and $\varphi_{ji}^{'}(r_{ji}) = \varphi_{ij}^{'}(r_{ij})$. Therefore, the above equation becomes

$$\begin{aligned}\frac{\partial E_{tot}}{\partial x_i} &= \sum_{j=1}^{N} F_j^{'}(\rho_j)\frac{\partial \rho_j}{\partial x_i} + \frac{1}{2}\sum_{k\neq i}^{N} S_{ik}\varphi_{ik}^{'}(r_{ik})\frac{x_{ik}}{r_{ik}} \\ &+ \frac{1}{2}\sum_{j\neq i}^{N} S_{ij}\varphi_{ij}^{'}(r_{ij})\frac{x_{ij}}{r_{ij}} + \frac{1}{2}\sum_{j=1}^{N}\sum_{k\neq j}^{N}\varphi_{jk}(r_{jk})\frac{\partial S_{jk}}{\partial x_i}.\end{aligned} \tag{3.7}$$

Because the summations in the second and third terms both go from 1 to N and both skip over i, they can be combined into a single summation, which leads to

$$\begin{aligned}\frac{\partial E_{tot}}{\partial x_i} &= \sum_{j=1}^{N} F_j^{'}(\rho_j)\frac{\partial \rho_j}{\partial x_i} + \sum_{k\neq i}^{N} S_{ik}\varphi_{ik}^{'}(r_{ik})\frac{x_{ik}}{r_{ik}} \\ &+ \frac{1}{2}\sum_{j=1}^{N}\sum_{k\neq j}^{N}\varphi_{jk}\frac{\partial S_{jk}}{\partial x_i}.\end{aligned} \tag{3.8}$$

The expressions for $\frac{\partial E_{tot}}{\partial y_i}$ and $\frac{\partial E_{tot}}{\partial z_i}$ are obtained by replacing x in Equation (3.8) with y or z. Then substituting the results into Equation (3.3), we can get Equation 3.1.

Unfortunately, the mathematical complexity of the background electron density and the screening function makes writing the expressions explicitly here impractical.

After the expression of the force had been obtained, we need to ensure its accuracy so that it can be used in the MEAM-MD program *mumeas.f*. A system of five Au atoms and a system of five Si atoms were created and these two systems were then used as input into *mumeas.f* and the forces acting on each atom were compared to those calculated by the Maple 7 program. The calculation showed that the results from the two programs agreed, verifying that *mumeas.f* could correctly evaluate Equation 3.1. Table 3.3 shows the calculated forces acting on each atom in these two systems.

Maple 7	F_x	F_y	F_z	*mumeas.f*	F_x	F_y	F_z
Au 1	-19.4118	-8.9018	-0.1544	Au 1	-19.4118	-8.9018	-0.1544
2	18.4355	-8.6644	-0.0151	2	18.4355	-8.6644	-0.0151
3	-0.0074	15.0816	0.0425	3	-0.0074	15.0816	0.0425
4	0.5862	1.3290	23.7494	4	0.5862	1.3290	23.7494
5	0.3975	1.1556	-23.6223	5	0.3975	1.1556	-23.6223
Si 1	-19.3372	-9.5439	-0.1886	Si 1	-19.3372	-9.5439	-0.1886
2	18.2756	-9.1768	-0.0004	2	18.2756	-9.1768	-0.0004
3	0.0669	16.2658	0.0712	3	0.0669	16.2658	0.0712
4	0.6177	1.3381	23.1030	4	0.6177	1.3381	23.1030
5	0.3770	1.1168	-22.9852	5	0.3770	1.1168	-22.9852

Table 3.3: Comparison of forces calculated by Maple 7 and *mumeas.f*. Values are given in eV/Å.

Chapter 4

Results

Once it had been established that the programs could correctly evaluate the MEAM equations, molecular dynamics simulations were performed. This chapter discusses results from these simulations, including the Si(100) surface reconstruction and adsorption of Au atoms on the Si(100) surface at room temperature. Similar studies were also performed at higher temperatures, such as 350 K, 800 K and 1200 in order to study the influence of temperature on Au/Si interactions. When discussing the results of the simulations, we focused on how the coverage and temperature affected the structure, morphology and surface stress of the Au layers. The time step in the molecular dynamics simulations was 4.125 fs. There were 100000 steps during the simulation, corresponding to a simulation length of 41.25 ps.

4.1 Simulations of Si(100) Reconstruction

4.1.1 Si(100) Relaxation at 0K

The first step of our study was to calculate the inter-layer relaxations of the Si(100) surface at 0 K. Inter-layer relaxations are changes in the atomic spacing between layers

as the system relaxes to equilibrium at 0 K. In our simulations, the Si substrate slab size was 8×8×8 with periodic boundary conditions applied in the ⟨100⟩ and ⟨010⟩ directions. To mimic bulk conditions, the atoms in the bottom two layers of the Si(100) substrate were fixed at the positions in the reference structure. Under this condition, it was considered that the fixed bottom atoms were too far off to interact with the atoms above the fixed region; therefore, the substrate could then be viewed as extending indefinitely like a bulk. All the Si atoms were initially positioned in a diamond lattice with an inter-layer spacing of 1.357 Å. Since at 0 K, the atoms had minimal thermal vibrations and their movement was restricted in the x and y direction because of the periodic boundary conditions, the atomic separations in the x and y directions were not changed after the relaxation. The inter-layer relaxation did however increase by 6.2% between the first and second layer, 0.7% between the second and third layer and 0.0% between the other layers. Calculations of the system energy showed that the surface energy decreased from 0.103 eV/Å^2 to 0.099 eV/Å^2 and the total energy decreased from -2274 eV to -2277 eV after relaxation.

In the bulk, the equilibrium distance between two layers is determined by various attractive and repulsive forces in the solid. When the surface is created, this balance is destroyed and the atoms at the surface therefore relax either inwards or outwards [43]. Our result shows that the Si(100) surface experienced an outward relaxation at 0 K, indicating the atomic separation in z direction was increased. Because the Si atoms did not move in the x or y direction, the separation of the atoms was increased, causing a weaker interaction between the atoms. At 0 K, the energy of the system mainly came from the atomic interactions; therefore, these outward relaxations reduced the surface energy and hence were energetically favorable.

4.1.2 Si(100) Reconstruction at 293K

Once conjugate gradient minimization had found the Si(100) relaxation at 0 K, the results were used as initial conditions to calculate the Si(100) reconstruction at 293 K with molecular dynamics. The bottom two layers were fixed as discussed in Section 4.1.1.

The output showed that the Si(100) surface had spontaneously reconstructed by forming dimers along the ⟨110⟩ direction (Figure 4.1). Spontaneous reconstructions suggested that a lower energy atomic configuration existed. Table 4.1 compares the 0 K surface energies, total energy of the system and inter-layer relaxations of Si(100) when in the reference structure, once relaxations had been considered and after reconstructing. σ is the surface energy while E_{tot} is the total energy of the system. Δ_{ij} is the inter-layer relaxation between layer i and layer j.

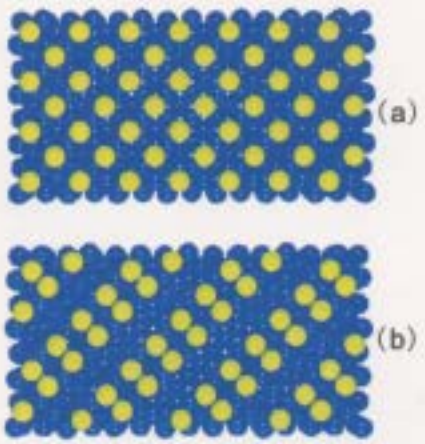

Figure 4.1: Si(100) substrate (a) before reconstruction and (b) after reconstruction at 293 K. The surface atoms are shown in yellow. The bulk atoms are shown in blue.

The formation of dimers during the Si(100) surface reconstruction indicates that when the surface is created by cleaving the bulk, some dangling bonds with higher energy are formed. This higher energy can be lowered during reconstruction when Si atoms bind together to form dimers. These dimers that form along the ⟨110⟩ direction have been observed in experiments [44, 45] and calculations [46, 47, 48]. In the STM experiments, Wolkow observed the asymmetric Si dimers during Si(100) reconstruc-

Table 4.1: Surface energy, total energy and inter-layer relaxations of Si(100) for various atomic configurations. Values for the surface energy are given in eV/Å^2. Values for the energy are given in eV. Values for inter-layer relaxations are expressed as a percentage of the equilibrium separation.

Configuration	σ	E_{tot}	Δ_{12}	Δ_{23}	Δ_{34}
Reference	0.103	-2274			
Relaxed	0.099	-2277	+6.2	+0.7	+0.0
Reconstructed	0.065	-2290	-2.5	+2.7	+0.6

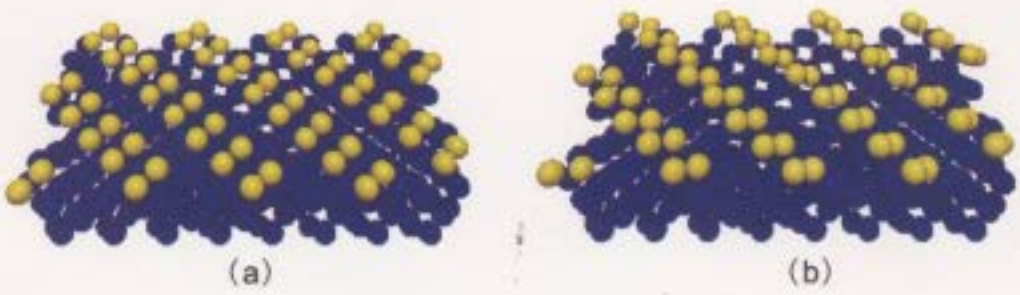

Figure 4.2: Configurations of the (a) symmetric(unbuckled) and (b) asymmetric(buckled) Si dimers on the Si(100) substrate.

tion at 120 K, while these dimers changed the orientation to get an average symmetric appearance at room temperature[44]. Tromp *et al.*'s studied atomic structure of the clean Si(100) surface. The samples were heated to 1323 K during 2 minutes and then cooled down gradually during 3-4 minutes. The STM images showed both symmetric and asymmetric dimers appeared in almost equal proportions [45]. It was explained in their study that the energies of the symmetric and asymmetric dimers were nearly degenerate and might be present at the same time. In Figure 4.2, we show the Si dimers on the reconstructed Si(100) surface. The Si dimers are shown in yellow while the other Si atoms are shown in blue. Figure 4.2(a) shows the Si dimers which are symmetric with respect to the ⟨110⟩ direction. Figure 4.2 (b) gives an example of the configurations for the asymmetric Si dimers on the Si(100) substrate. We can see in

each of these Si dimers, the Si atom at the left hand side is above the Si(100) surface, ruining the symmetry of the dimer along ⟨110⟩ direction in the Si(100) surface plane. In our simulation, the symmetric Si dimers as shown in Figure 4.2(a) were observed, consistent with results calculated by Baskes [46], but in contrary with first principle calculations [47, 48] which observed asymmetric dimers buckled inward or out of the Si(100) surface. As the experiments observed both symmetric and asymmetric dimers at the same time, these different calculations may have shown different behaviors of the system during Si(100) reconstruction.

4.2 Simulations of Au Layers on the Si(100) Substrate

In this section, we placed Au atoms on Si(100) surface at various coverages and temperatures. The initial separation distance between the bottom Au layer and the Si(100) surface was approximately 3.0 Å for all the simulations in this study; however, this distance is not critical because the system can relax to the same equilibrium even if the initial conditions are slightly different [29].

4.2.1 Au Layers on the Reconstructed Si(100) Substrate at 293 K

We first placed 6.7% ML[1] Au on a reconstructed Si(100) substrate at 293 K, and then increased the coverage to 21.3%, 33.3%, 42.7% and 66.7%. The initial positions and velocities of Si atoms were determined by the output of the previous analysis

[1] 1 ML is defined as 15×10 Au atoms in the fcc(111) configuration, corresponding to 100% coverage of Au atoms on Si(100) surface. The number of Au atoms in the x and y direction was chosen according to the size of the box in periodic boundary conditions.

discussed in section 4.1.2.

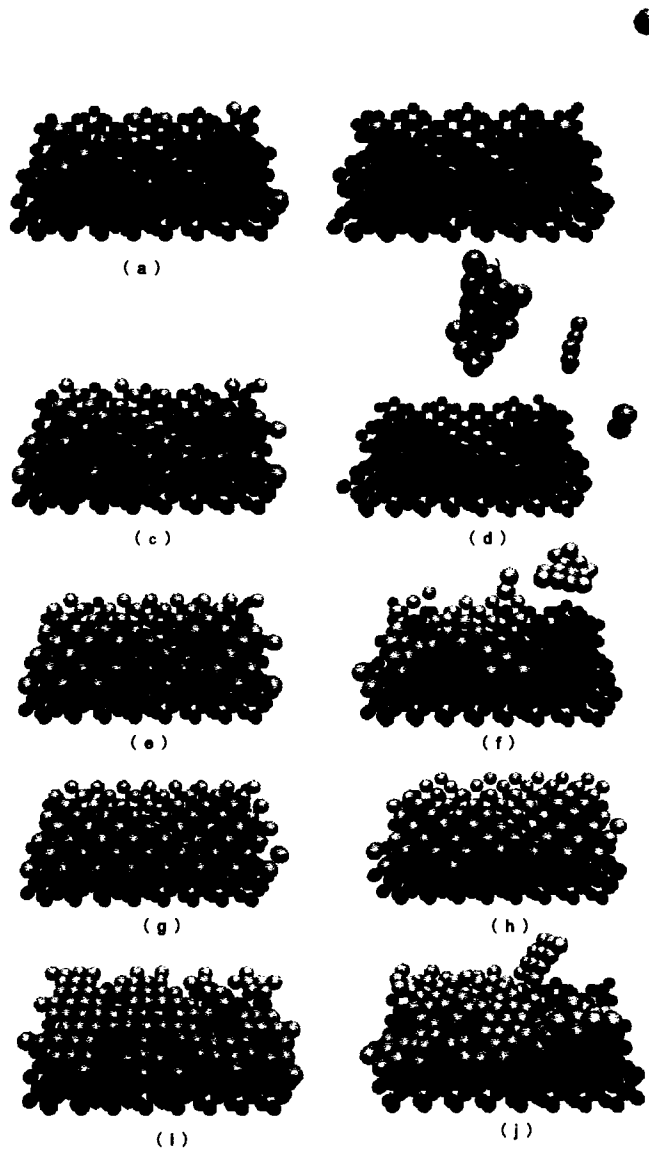

Figure 4.3: Au atoms on the reconstructed Si(100) substrate at 293K below 1 ML coverage. Initial configurations of the system when the Au coverage is (a)6.7% (c)21.3% (e)33.3% (g)42.7% (i)66.7%. Final configurations of the system when the Au coverage is (b)6.7% (d)21.3% (f)33.3% (h)42.7% (j)66.7% ML.

Figure 4.3 shows the initial and final configurations at 41.25 ps for Au atoms on a reconstructed Si(100) substrate below 1 ML coverage. The Au atoms are shown in yellow, the reconstructed Si(100) surface is shown in green and the other Si atoms are shown is blue. When the Au coverage was low (6.7% and 21.3%), most Au atoms re-evaporated from the substrate at the end of the simulations(Figure 4.3(b)(d)). At 33.3% coverage, about half of the Au atoms re-evaporated (Figure 4.3(f)). Figure 4.3(h) shows when 42.7% ML Au with reflecting symmetry along the x and y axis was placed on the substrate, all the Au atoms could stay on the Si(100) surface. In Figure 4.3(i), we can see when the coverage was increased to 66.7%, but with lower symmetry, there were still Au atoms re-evaporated at the end of the simulation. As we collected these results at 41.25 ps when re-evaporation was still going on, it can be expected that if the simulation time had been longer, all the Au atoms might evaporate from the substrate. To confirm this speculation, we increased the simulation time to 200 ps and re-ran these programs. It was found that below 42.7% Au coverage, fewer Au atoms stayed on the Si substrate (Figure 4.4 (a)) while at 42.7% and 66.7%, all the Au atoms stayed at the Si substrate (Figure 4.4 (b)(c)) at the end of the simulations.

According to our simulations, re-evaporation of the added atoms on the substrate does occur as discussed in Reference [49]. It is illustrated in Chapter 6 of Reference [49] that the energy state of the substrate is energetically like an egg carton, with the energy depressions constituting temporary adsorption sites for the deposited atoms. When an added atom comes into one of these sites, it will either hop out of the egg carton, i.e. re-evaporate, or jump over the energy barrier into an adjacent site and bind with another atom to form a doublet making the atoms more stable than the single atoms. In our simulations, generally, the Au atoms became more stable on the Si substrate at a higher Au coverage. Based on the statement in Reference [49], this

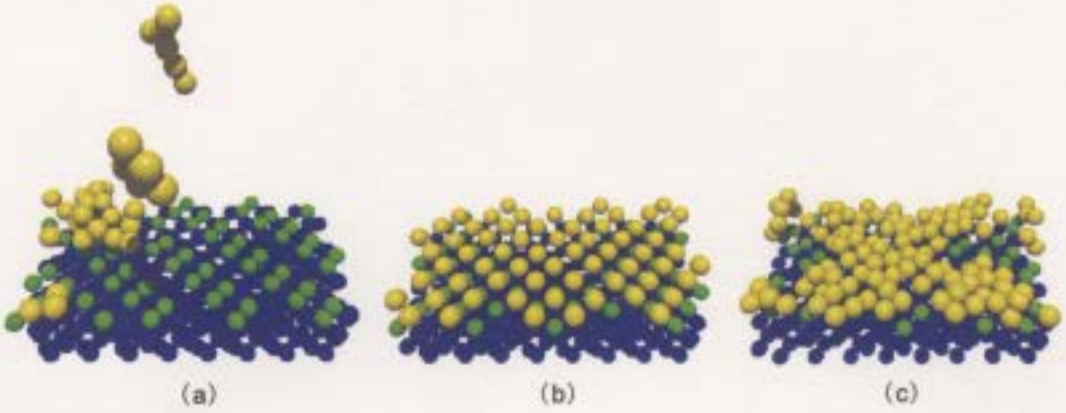

Figure 4.4: Final configurations of (a) 33.3% (b) 42.7% and (c) 66.7% Au atoms on the reconstructed Si(100) substrate at 200 ps.

result can be explained as follows: when the Au coverage was low, the interactions between the Au atoms and other atoms were limited; thus, it was more difficult for a Au atom to bind with another atom and form a doublet. When the Au coverage was higher, there were more interactions between the atoms so that the chance for a Au atom to bind with the other atoms was increased. Also, it was possible that the deposited Au atoms could modify the energy state of the surface by increasing the available adsorption sites; hence, more Au atoms could stay on the Si surface without re-evaporation.

We next performed simulations of Au layers with coverages from 1 ML to 3 ML on the Si(100) surface. Again, the Au layers were constructed as an fcc(111) crystal structure with 15 atoms in the x direction and 10 atoms in the y direction. Figure 4.5, Figure 4.6 and Figure 4.7 show the initial and final configurations of the system. In these figures, (a) and (d) show the front view, and (b) and (e) show the side view of the initial and final configuration. In (c) and (f), the configuration of the Si surface beneath the Au layers is displayed: the Si surface atoms are shown in green while the Au layer on top of the Si surface is shown in yellow, both seen from the $+z$ direction.

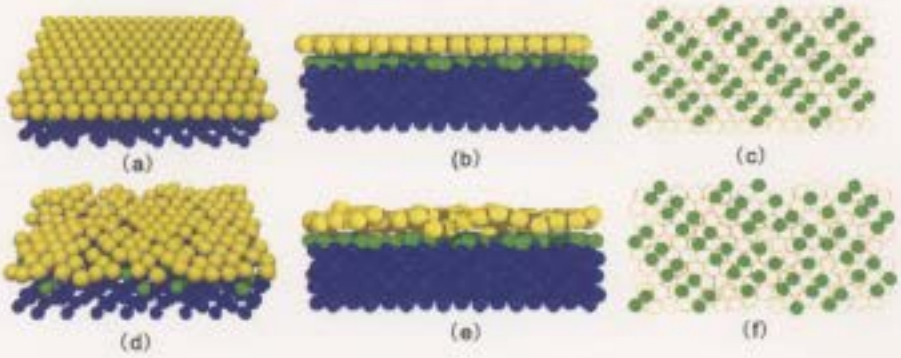

Figure 4.5: 1 ML Au on the reconstructed Si(100) at 293K. Front view of the (a) initial and (d) final configuration. Side view of the (b) initial and (e) final configuration. (c) Initial and (f) final configuration of the Si surface beneath the Au layers.

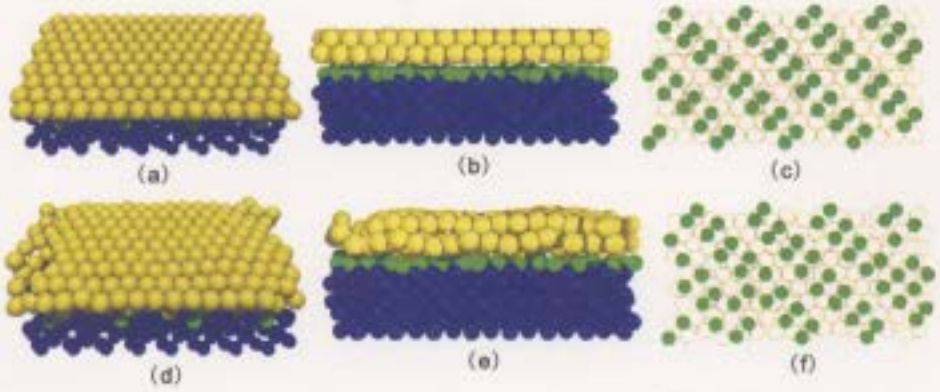

Figure 4.6: 2 ML Au on the reconstructed Si(100) at 293K. Front view of the (a) initial and (d) final configuration. Side view of the (b) initial and (e) final configuration. (c) Initial and (f) final configuration of the Si surface beneath the Au layers.

In these figures, Figure 4.5(d) shows that when the Au coverage was 1 ML, the crystal lattice was significantly perturbed, while in Figure 4.6(d) and Figure 4.7(d), the crystal lattice was slightly perturbed at 2 and 3 ML Au coverage. In Figure 4.7(e), we can see at 3 ML coverage the Au layers expand in z direction within the simulation time of 41.25 ps. Figure 4.5(f), 4.6(f) and 4.7(f) show at the end of the simulation there were still Si dimers on the Si(100) surface.

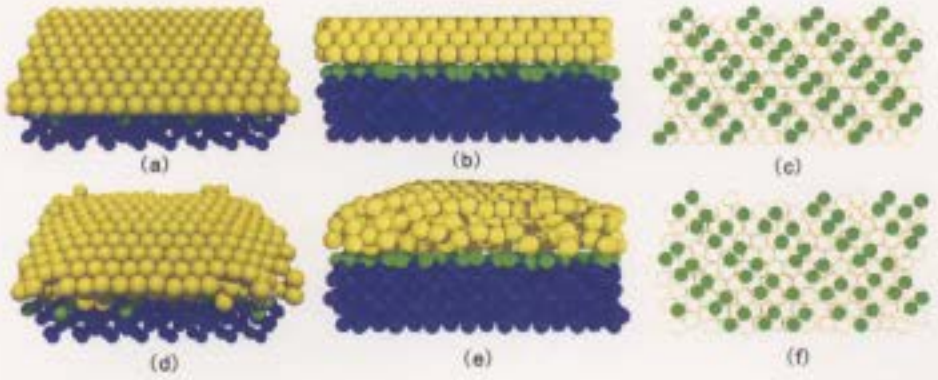

Figure 4.7: 3 ML Au on the reconstructed Si(100) at 293K. Front view of the (a) initial and (d) final configuration. Side view of the (b) initial and (e) final configuration. (c) Initial and (f) final configuration of the Si surface beneath the Au layers.

Many papers have reported Au/Si intermixing and the formation of amorphous gold silicide layers above a certain critical coverage [4-7,10,11,13,17] ; however, these experiments disagree in the required critical coverage to initiate Au/Si intermixing. Narusawa *et al.* reported that the intermixing started abruptly when the Au film exceeded a critical coverage of 4 ML [5]. Carriere *et al.* reported the Au silicide was formed when 2 ML Au coverage was achieved[6] while Hricovini *et al.* suggested that Au and Si started intermixing below 1 ML [7]. In our simulations, when the Au coverage was below 3 ML, no intermixing was observed within 41.25 ps; therefore, it can be speculated that the critical coverage might be above 3 ML, so that the number of Au layers was not enough to start intermixing. Also, it is possible that the time duration of 41.25 ps might be too short to observe intermixing between Au layers and the Si substrate. Au/Si intermixing may be observed if the simulation time is increased. To verify these speculations, simulations for larger systems and longer simulation time need to be performed in the future work.

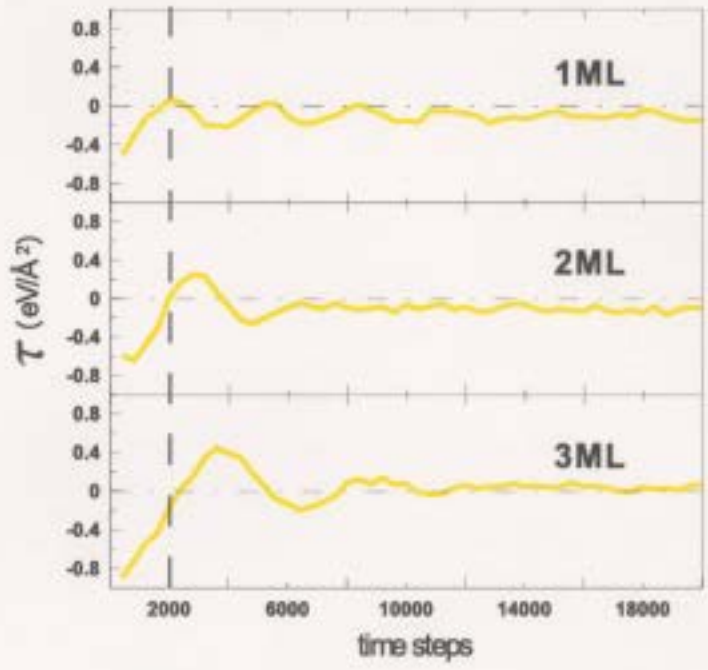

Figure 4.8: Direct surface stress τ_{zz} as a function of time in the first 20000 time steps. The unit of surface stress is eV/Å^2. The unit of x axis is time step (1 time step = 0.4125fs).

The surface stress of the system was recorded during the simulations. Figure 4.8 shows the direct stress τ_{zz} as a function of time in the first 20000 steps. It can be noticed that for different coverages, in the first 2000 time steps, τ_{zz} had large negative values, indicating that the surface tended to expand in $+z$ direction at the beginning of the simulation. Then τ_{zz} reached a nonnegative maximum and became 0 after 100000 time steps, suggesting the direct surface stress in z direction might be zero when the system reached equilibrium.

Figure 4.9 shows the evolution of surface stress at different Au coverages within 100,000 time steps, which correspond to a simulation time of 41.25 ps. This graph shows the surface stresses oscillated intensively in the first 20,000 time steps, indicating the system was far from equilibrium at the beginning of the simulation; therefore,

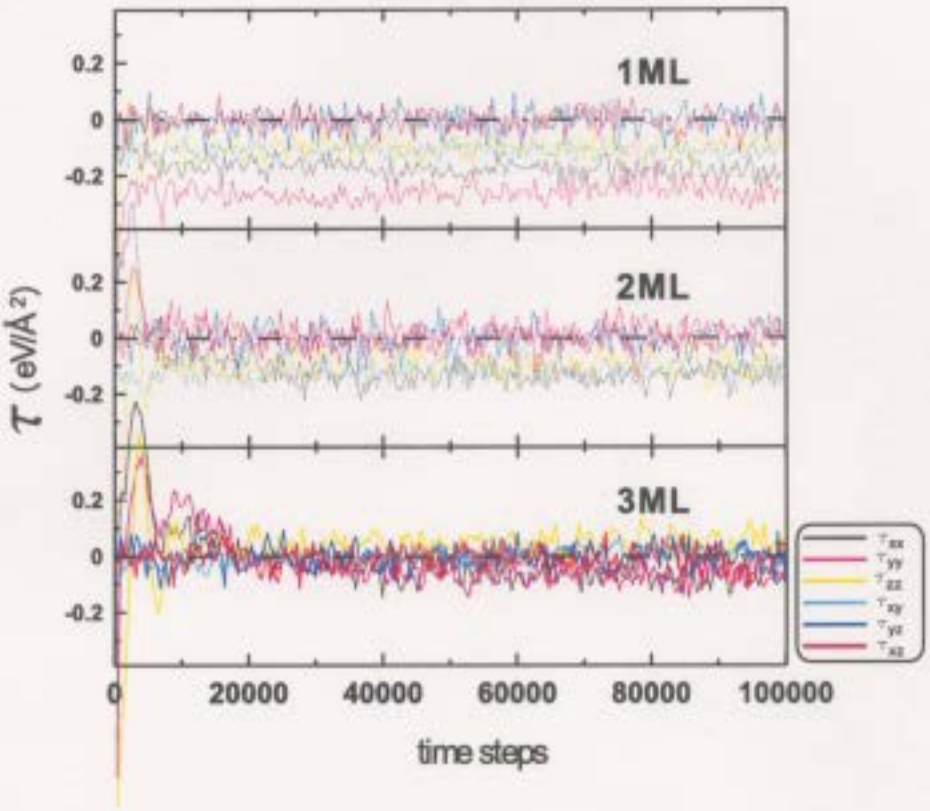

Figure 4.9: Evolution of the surface stress when Au atoms were placed on the reconstructed Si(100) substrate at 293 K. The unit of surface stress is eV/Å^2. The unit of x axis is time step (1 time step = 0.4125fs).

the atoms had to move around with large displacement to adjust themselves towards the equilibrium. With the increase of Au coverage, the amplitude of oscillation at the beginning increased; thus, at higher Au coverage, the atoms in the system took more effort to adjust themselves during equilibrating. After 20,000 time steps, the surface stress fluctuated with a smaller amplitude and became more stable until the end of the simulation. The calculations of surface stress show that at 1 ML Au coverage, the average values of τ_{xx} and τ_{yy} are -0.1729 eV/Å^2 and -0.2650 eV/Å^2, respectively. From Figure 4.9, we can see compared with the other surface stress elements, τ_{xx} and τ_{yy} have lager distances away from the black dashed line which denotes the zero

surface stress, indicating that the system had larger direct surface stresses in the x and y direction. When the coverage was increased to 2 ML, all the elements in the surface stress tensor were closer to 0. Figure 4.9 shows that τ_{xx} has the largest value and its average is -0.1028 eV/Å^2 according to the calculations. At 3 ML coverage, we can see from Figure 4.9 all the surface elements are around 0. The calculation of surface stress elements shows in the six surface stress elements, τ_{zz} has the largest average value which is 0.0348 eV/Å^2. According to our results, when Au atoms were placed on the Si(100) surface at 293 K, the surface stress became smaller at higher Au coverage.

4.2.2 Au Layers on the Unrelaxed Si(100) Substrate at 293 K

In Kuo and Clancy's study, the Au layers were placed on the unrelaxed Si(100) (i.e. reference structure) at the beginning of the simulations. This initial condition could simplify the simulations since no Si(100) relaxation or reconstruction were calculated. In this section, we placed the Au layers on the unrelaxed Si(100) surface at 293 K and compared the simulations with those in section 4.2.1.

According to the results, there is no significant change in the morphology of the Au layers or the surface stress (Figure 4.10 and Figure 4.11). Figure 4.12 shows that no intermixing was observed within 41.25 ps when Au atoms were placed on the unrelaxed Si(100) surface below or at 3 ML coverage at 293 K.

In Figure 4.13, the configuration of the Si surface beneath the Au layers is displayed. The Si surface atoms are shown in green while the Au layer on top of the Si surface is shown in yellow, as discussed in the last section. Figure 4.13(a) shows the initial configurations while (b), (c) and (d) show the final configurations of these

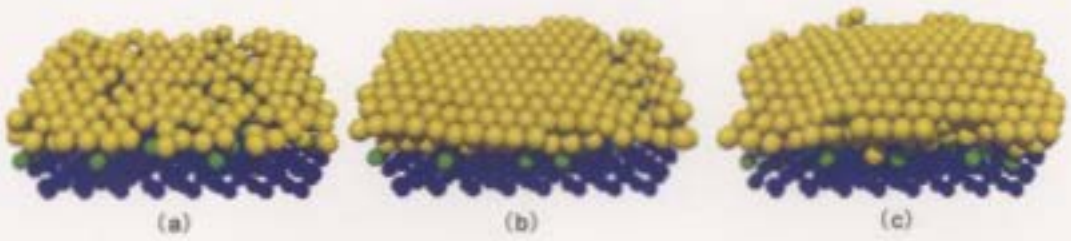

Figure 4.10: Front view of the final configurations for (a) 1 ML (b) 2 ML and (c) 3 ML Au on the unrelaxed Si(100) substrate at 293 K.

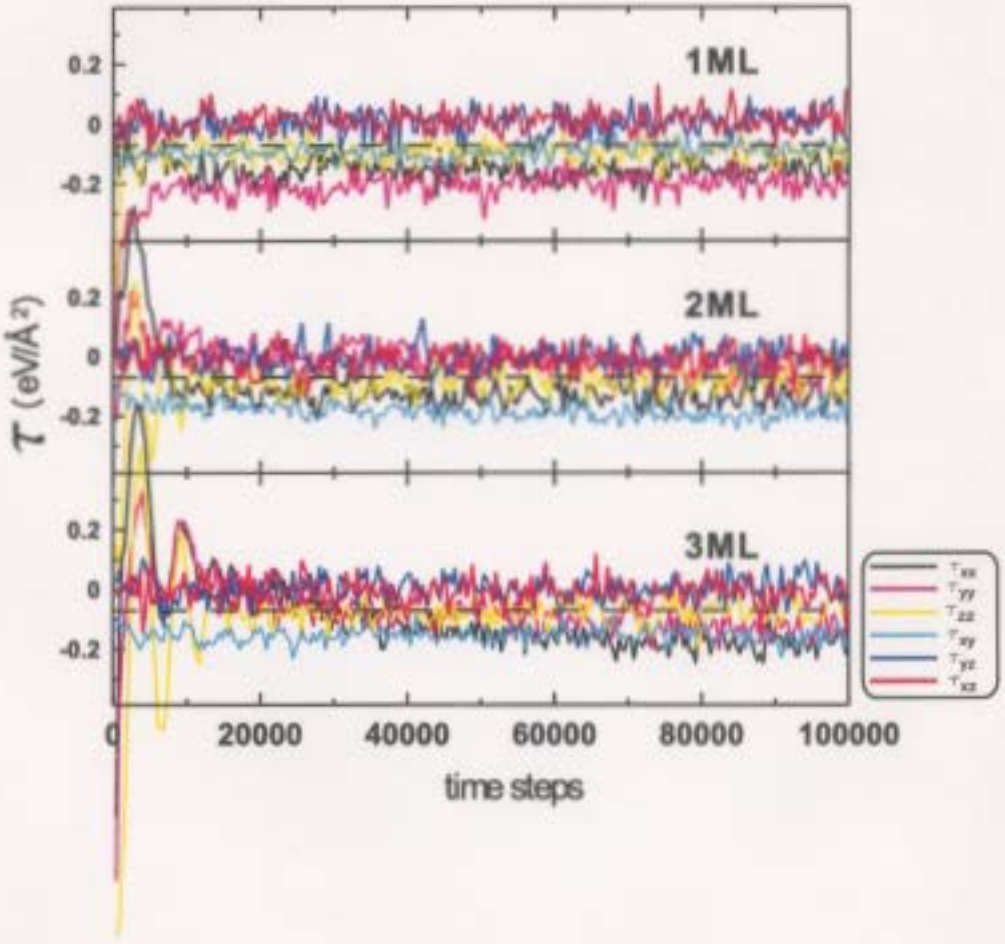

Figure 4.11: Evolution of the Surface Stress when Au atoms were placed on the unrelaxed Si(100) substrate at 293 K.

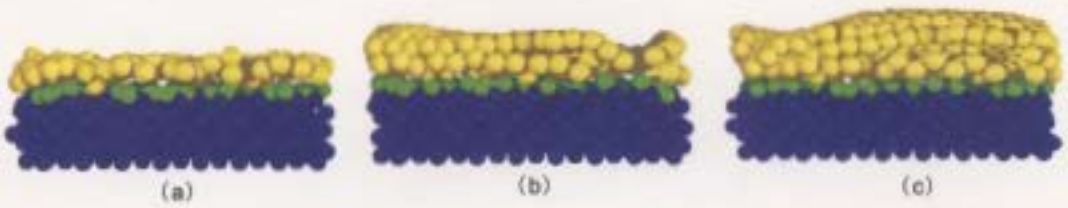

Figure 4.12: Side view of the final configurations for (a) 1 ML (b) 2 ML and (c) 3 ML Au on the unrelaxed Si(100) substrate at 293 K.

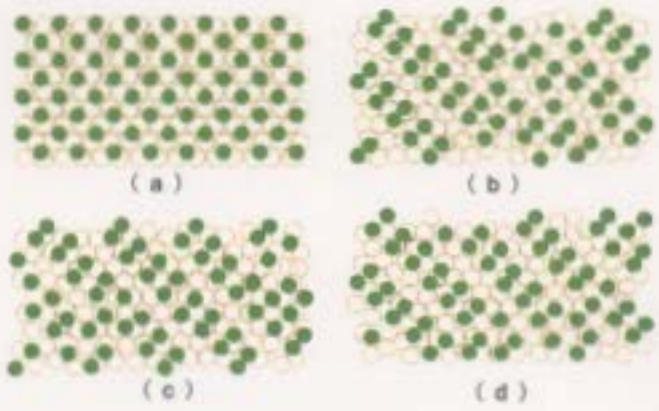

Figure 4.13: (a) Initial and final configurations of the Si(100) surface below the Au layers when (b) 1 ML (c) 2 ML (d) 3 ML Au were placed on the unrelaxed Si(100) substrate at 293 K.

two Si and Au layers at different Au coverages. We can see that the Si surface still reconstructed by forming dimers even though there were no dimers on the Si(100) surface at the beginning of the simulation, suggesting Au atoms did not prevent the formation of Si dimers on the Si(100) surface in the first 41.25 ps of the simulation.

Table 4.2 compares the total energy, surface energy, potential energy and kinetic energy of the system at the end of the simulations of Au layers on the unrelaxed and reconstructed Si(100) substrate. The first 5 columns show these energies when the Au atoms were placed on the unrelaxed Si(100) substrate, while the following five columns show those when the Au atoms were placed on the reconstructed Si(100)

unrel.	E_{tot}	σ	E_{pot}	E_k	recons.	E_{tot}	σ	E_{pot}	E_k
1 ML	-3097	-0.1718	-3122	25.02	1 ML	-3077	-0.1500	-3102	25.13
2 ML	-3578	-0.1866	-3608	29.60	2 ML	-3550	-0.1573	-3580	29.63
3 ML	-4098	-0.1802	-4132	34.65	3 ML	-4095	-0.1772	-4129	34.76

Table 4.2: Energy of the system when the Au atoms were placed on the unrelaxed and the reconstructed Si(100) substrate. The values of total energy, potential energy and kinetic energy are given in eV. The values of surface energy are given in eV/Å^2.

substrate. As we can see in Table 4.2, the kinetic energy of the system was the same for these two simulations since both simulations were taken at the same temperature. The total energy, the surface energy and the potential energy of the system were slightly smaller when the Au atoms were placed on the unrelaxed Si(100) substrate, indicating the total energy might be minimized even better under this condition.

4.2.3 Au Layers on the Reconstructed Si(100) Substrate with Unfixed Bottom Two Layers

In the previous simulations, the bottom two layers of the Si substrate were fixed to mimic a bulk sample. In this section, we unfixed the two bottom layers and compared the results with those in section 4.2.1 to see if they were affected. It was observed that the morphology of the Au layers and the configuration of the Si(100) surface beneath the Au layers were unaffected (Figure 4.14 and Figure 4.16). The side view of the Au layers on top of the Si substrate shows below 3 ML coverage at 293 K, still no intermixing was observed within 41.25 ps when Au atoms were placed on the reconstructed Si(100) surface with two bottom layers unfixed(Figure 4.15).

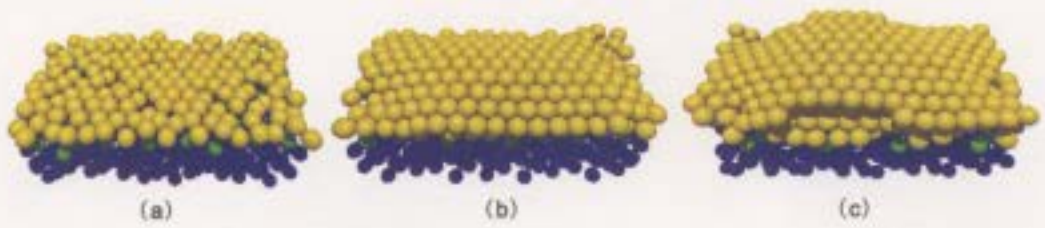

Figure 4.14: Front view of the final configurations for (a) 1 ML (b) 2 ML and (c) 3 ML Au on reconstructed Si(100) substrate with unfixed bottom two layers at 293 K.

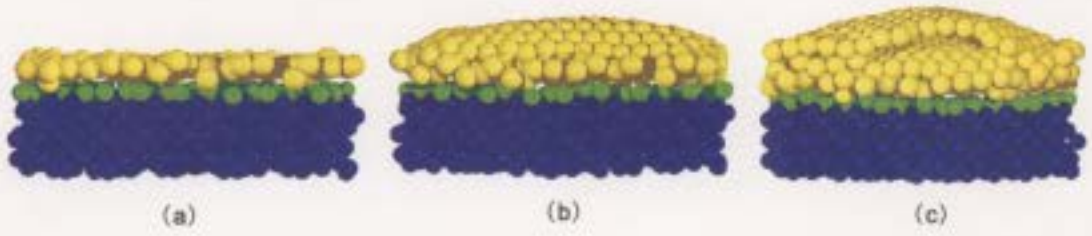

Figure 4.15: Side view of the final configurations for (a) 1 ML (b) 2 ML and (c) 3 ML Au on reconstructed Si(100) substrate with unfixed bottom two layers at 293 K.

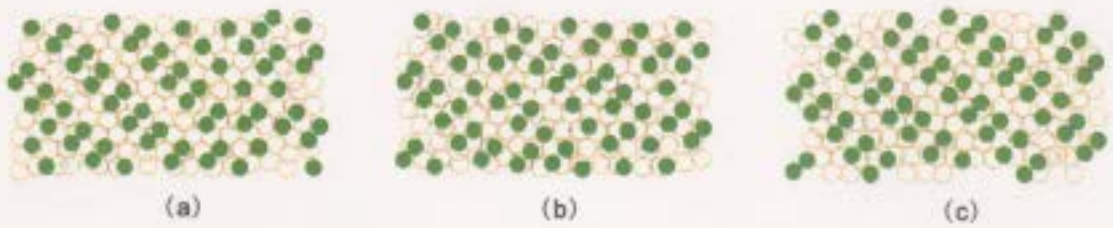

Figure 4.16: Final configuration of the Si(100) surface below the Au layers when (a) 1 ML (b) 2 ML (c) 3 ML atoms were placed on reconstructed Si(100) substrate with unfixed bottom two layers at 293 K.

Compared with the previous simulations in section 4.2.1, the most observable differences lie in the configuration of the bottom surface of the Si substrate and the surface stress of the system. Figure 4.17 shows when no atoms were fixed in the system, the bottom surface of the Si(100) substrate reconstructed by forming dimers, indicating the system could not be considered as a bulk under this condition.

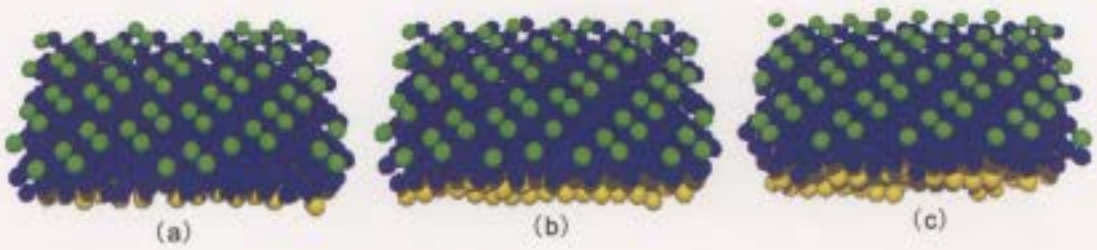

Figure 4.17: Reconstruction of the bottom surface when (a) 1 ML (b) 2 ML and (c) 3 ML Au were placed on the reconstructed Si(100) substrate with unfixed bottom two layers at 293 K.

Figure 4.18 shows the surface stress of the system in comparison with that in section 4.2.1, we can see all the elements in the surface stress tensor are closer to 0 than those when the bottom two Si layers were fixed, suggesting a smaller surface stress in the system. This result was expected because when the bottom two layers of the Si substrate were unfixed, the system had more freedom to adjust itself to the deformation; therefore, less surface stress could be induced.

4.2.4 The Influence of Temperature on the Au/Si Interaction

It has been reported that adsorption of Au atoms on the Si substrate can be influenced by temperature [15, 29, 50]. Yang *et al.*[15] studied the concentrations of the top layer after 4.17 ML Au atoms were deposited at 163 K and then annealed at 460 K. It was found that at the top layer, the Au concentration was close to 100%. Ceelen *et al.* [50] found that at lower coverage (a few monolayers), the Au composition was about 70% until the temperature was increased to 675 K. Increasing the temperature further resulted in a decrease of the Au concentration to 48%. This concentration stayed constant until the temperature was increased to 1025 K. In C. L. Kuo *et al.*'s simulations [29], after the Au thin films were annealed at 500 K, a crystalline Au top

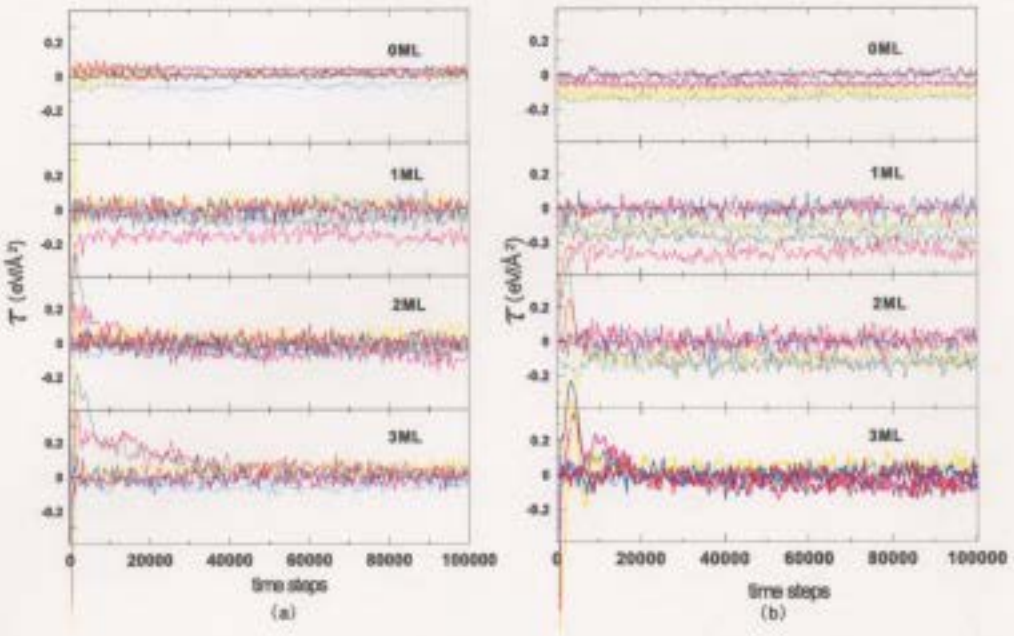

Figure 4.18: Evolution of the Surface Stress when Au atoms were placed on the reconstructed Si(100) substrate with bottom two layers (a) unfixed and (b) fixed at 293 K. The unit of surface stress is eV/Å^2. The unit of x axis is time step (1 time step = 0.4125fs).

layer was obtained. Between 600 K and 800 K, Si outdiffused significantly and the top layer became Si-rich. As the annealing temperature was increased from 800 K to 1000 K, Au atoms stopped to diffuse into the Si substrate. It was concluded that the growth of gold silicide was dominated by the outdiffusion of Si atoms above 600K.

In this section, the temperature of the system was increased to 350 K, 800 K and 1200 K by adjusting the velocities of the atoms based on the equipartition of energy principle discussed in 2.3.2. The system stayed at the desired temperature for a simulation time of 41.25 ps. The input for these simulations was the output of the simulations of Au atoms on the reconstructed Si(100) substrate at 293 K.

At 350 K, no intermixing was observed within the simulation time of 41.25 ps at 1, 2 and 3 ML Au coverage (Figure 4.19). Figure 4.20 shows that the morphology of

the Au layers was almost the same as that at 293 K and the Au concentration at the top layer was 100%.

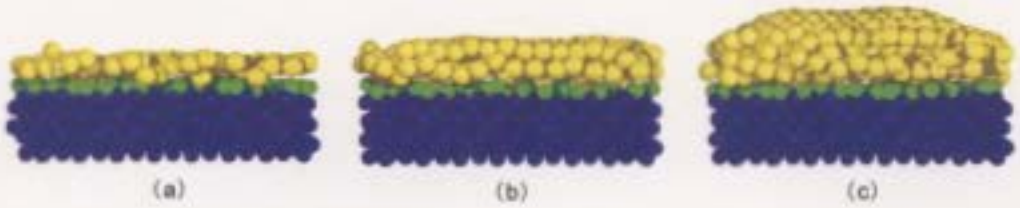

Figure 4.19: Side view of the final configurations of (a) 1 ML (b) 2 ML and (c) 3 ML Au on the reconstructed Si(100) substrate at 350 K.

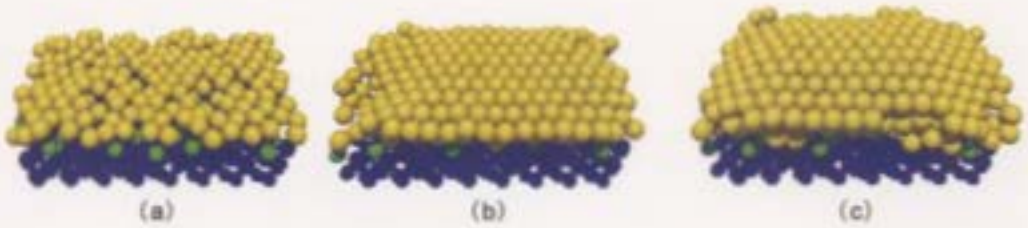

Figure 4.20: Front view of the final configurations for (a) 1 ML (b) 2 ML and (c) 3 ML Au on reconstructed Si(100) substrate at 350 K.

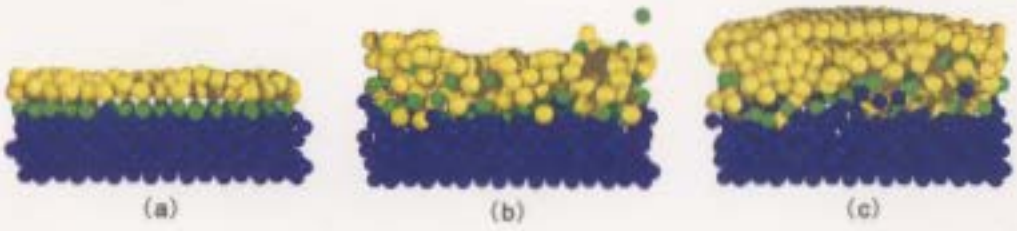

Figure 4.21: Side view of the final configurations of (a) 1 ML (b) 2 ML and (c) 3 ML Au on the reconstructed Si(100) substrate at 800 K.

Figure 4.21 shows the side view of the final configurations under different Au coverages at 800 K. We can see that at 1 ML coverage, no intermixing was observed by the end of the simulation. Figure 4.21 (b) shows when the Au coverage was 2 ML, Au

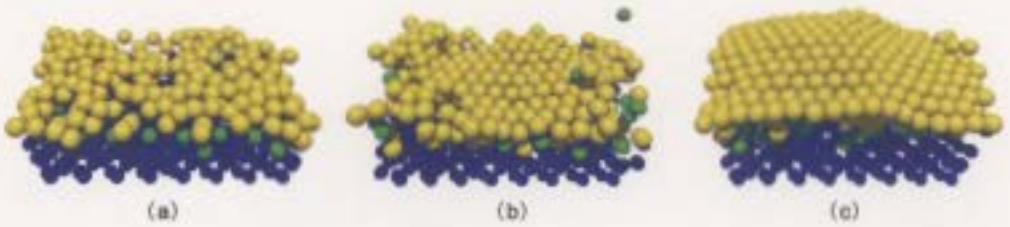

Figure 4.22: Front view of the final configurations for (a) 1 ML (b) 2 ML and (c) 3 ML Au on reconstructed Si(100) substrate at 800 K.

and Si atoms intermixed significantly, so that the interface between Si substrate and Au layers became obscure. Most of the intermixed Si atoms came from the substrate surface and some of them diffused out of the Au layers and evaporated. Figure 4.22(a) and (c) show that the top layer only consisted of Au atoms at 1 and 3 ML Au coverage. In Figure 4.22(b), several Si atoms appeared at the top surface when the Au coverage was 2 ML, but the top layer was still Au-rich. At 3 ML Au coverage, intermixing of Si and Au atoms was observed at the interface of Si substrate and Au layers, but no Si atoms were observed at the top layer or evaporated from the substrate within 41.25 ps. According to our results, below 3 ML Au coverage, intermixing of Au and Si atoms can be enhanced by increasing the temperature; whereas, the intermixing was not as much as reported by other experiments or simulations.

When the temperature was increased to 1200 K, evaporation of Au and Si atoms was observed below their melting points (1337 K for Au and 1687 K for Si). Figure 4.23, Figure 4.24 and Figure 4.25 show the evolution of the system at 1200 K. At 1 ML Au coverage, the atoms on the Si(100) surface not only diffused out of the Au layer and evaporated, but also diffused into the bottom region of the Si substrate, indicating that the diffusivity of the Si atoms was increased with higher temperature. The Au atoms started to evaporate from Si substrate at about 10 ps after the temperature was increased to 1200 K. During the evaporation, the distance between Au and Si

atoms was increased to above the cut-off distance during evaporation; therefore, there were no interactions between Au and Si atoms, so that the Au atoms interacted with each other and bonded together to form a sheet. Figure 4.24 shows that during the evaporation at 2 ML coverage, both the surface Si atoms and those in the substrate diffused out of the Au layers and evaporated. In Figure 4.24(c), melting at the Au and Si interface was observed at about 15 ps, followed by evaporation of the two Au layers when the simulation continued until 41.25 ps. Figure 4.25 shows that at 3 ML coverage, Au and Si interface still melted before the evaporation of the Au layers and it took more time for the Au layers to evaporate from the substrate than that when the Au coverage was 1 and 2 ML.

Evaporation of Au and Si atoms below their melting points remains as a question in this study. It is hard to explain how Au atoms could obtain so much energy to get rid of interactions with Si atoms and leave the Si substrate. It is possible that our cut-off distance might be too small to include interactions with in larger distances, or the MEAM parameters for the Au/Si system need to be modified when the temperature was increased to 1200 K.

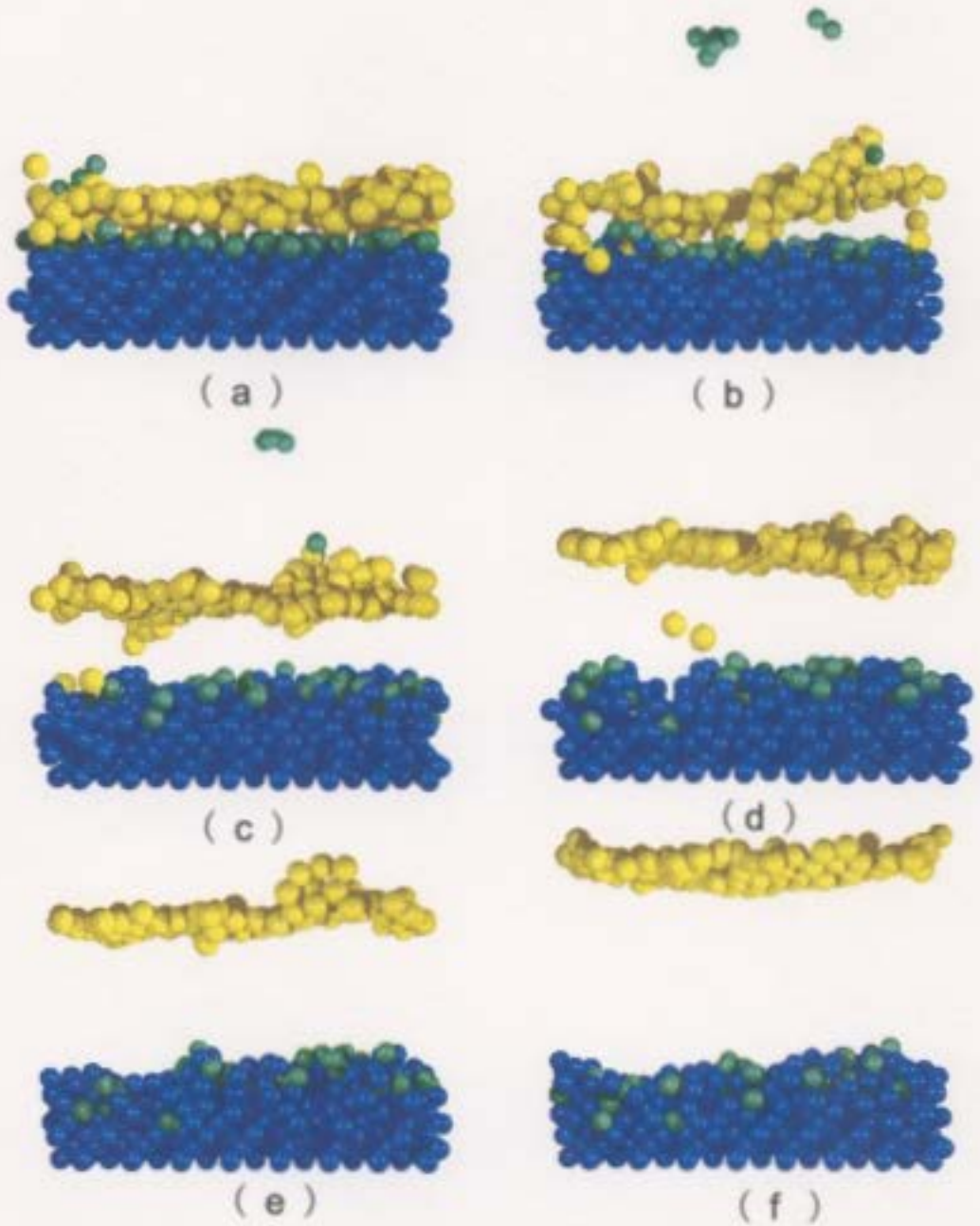

Figure 4.23: Side view of the configurations at (a) 4.95ps (b) 9.90ps (c) 14.85ps (d) 21.45ps (e) 29.37ps (f) 41.25ps for 1 ML Au on the reconstructed Si(100) substrate at 1200 K.

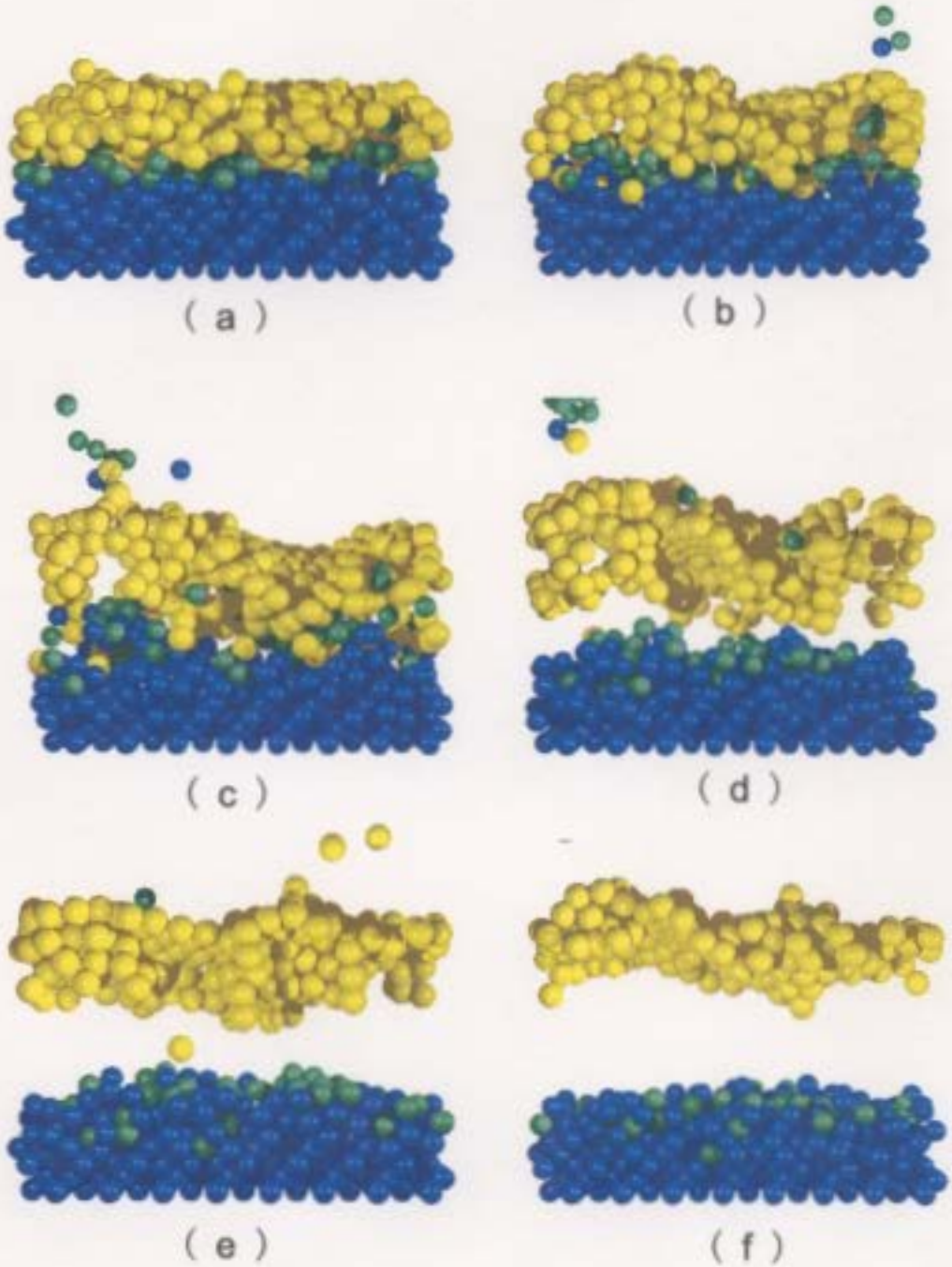

Figure 4.24: Side view of the configurations at (a) 4.95ps (b) 9.90ps (c) 14.85ps (d) 21.45ps (e) 29.37ps (f) 41.25ps for 2 ML Au on the reconstructed Si(100) substrate at 1200 K.

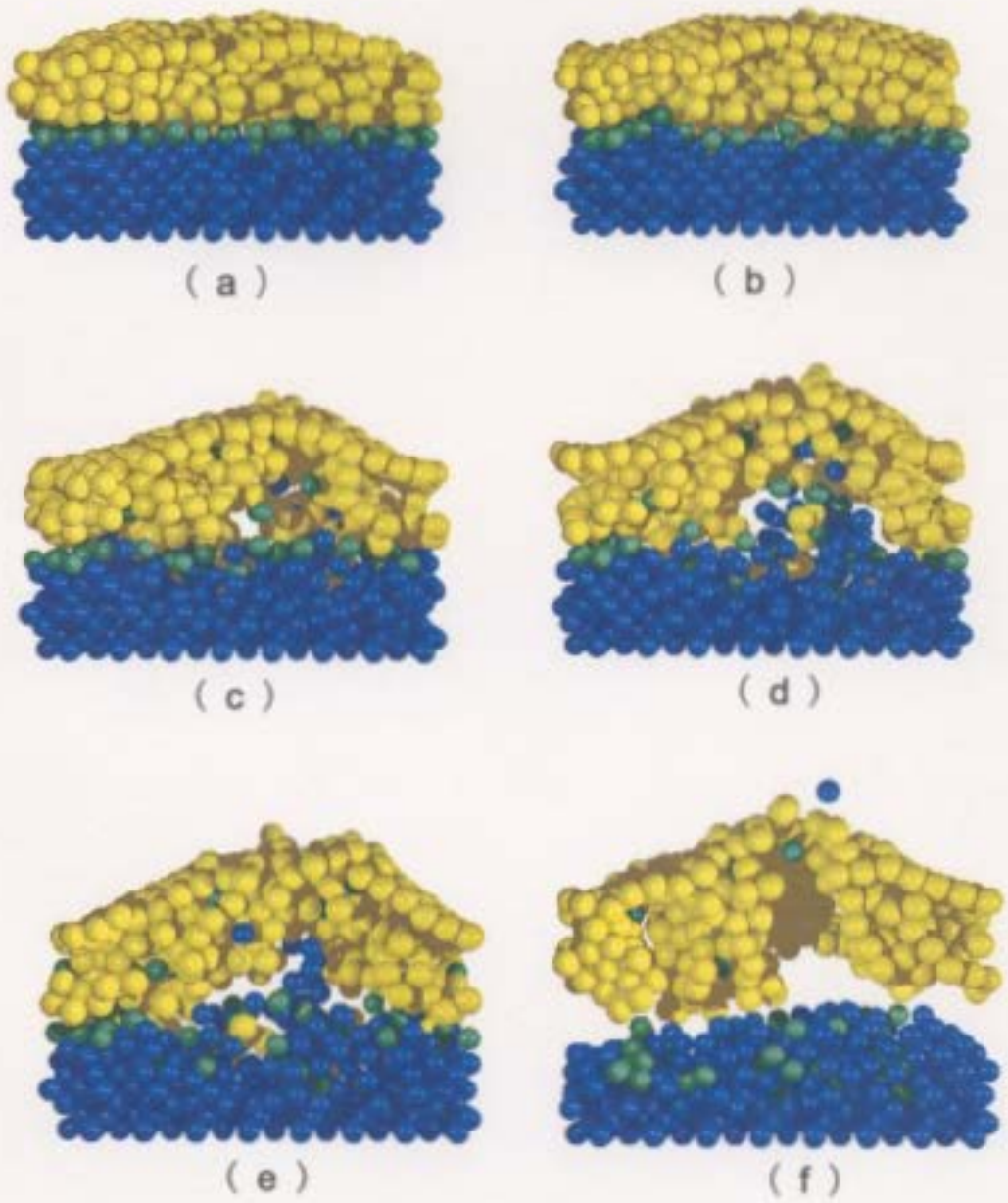

Figure 4.25: Side view of the configurations at (a) 4.95ps (b) 9.90ps (c) 14.85ps (d) 21.45ps (e) 29.37ps (f) 41.25ps for 3 ML Au on the reconstructed Si(100) substrate at 1200 K.

Chapter 5

Conclusions

5.1 Conclusions

In this thesis, molecular dynamics simulations using MEAM models were applied to study the Si(100) reconstruction and Au/Si interactions. The results showed the Si(100) substrate relaxed by moving Si surface atoms in the z direction at 0 K, resulting in an increase of the inter-layer separations. At 293 K, the Si(100) surface reconstructed by forming dimers in the $\langle 110 \rangle$ direction, consistent with Baskes's MEAM calculations of the Si(100) reconstruction [46]. Simulations of Au atoms on the reconstructed Si(100) substrate showed that Au atoms re-evaporated from the Si surface below 1 ML coverage, and became more stable when the coverage was increased. At 1, 2 and 3 ML Au coverage, all the Au atoms stayed on the Si substrate without re-evaporation although no Au/Si intermixing was observed within the simulation time of 41.25 ps. We also calculated the surface stress of the system at different Au coverages. According to the results, the surface stress oscillated intensively at the beginning of the simulations and became stable when the system approached equilibrium. Comparing the surface stress of the system at different Au coverages, we

found that the surface stress became smaller when the Au coverage was increased. The system had the largest nonignorable surface stress at 1 ML Au coverage when the morphology was quite different from that at 2 and 3 ML Au coverage (Figure 4.5-4.7). This result implied that the surface stress was related to the morphology of the Au film as shown in Figure 1.5. Lastly, we studied the influence of temperature on the Au/Si interactions. It was observed that Au and Si intermixed above 2 ML Au coverage at 800 K, suggesting the Au/Si interdiffusion could be enhanced by increasing the temperature. At 1200 K, melting of the Au/Si interface followed by evaporation of both Au and Si was observed.

5.2 Future work

In future work, we will simulate the deposition process of Au atoms on the Si substrate by considering the deposition parameters, such as the deposition rate which is the amount of the atoms deposited per unit time, and the velocities of the Au atoms when they arrive at the Si substrate, which are controlled by the power source . Considering these initial conditions requires lengthy simulations because the system may be too far from equilibrium and the deposition time can be longer than several minutes. We will also study how the film thickness influences the Au/Si interactions at higher Au coverages; therefore, simulations of longer simulation time and larger systems will be performed requiring programs with higher efficiencies. Hence, parallel programs may be developed to achieve high-speed calculations.

Since the substrate temperature and the post-deposition annealing temperature play significant roles in thin film synthesis, we will perform simulations at various temperatures. However, as the MEAM parameters were calculated at 0 K and an imaginary NaCl structure was used as the Au/Si reference structure, their accuracy

can be questioned. In our future work, we hope to calculate our own parameters, so that MEAM parameters for higher temperature and various phase structures can be obtained.

Also, we will investigate the effects of using different intermediate tie layers between the Au layers and the Si substrate. In experiments, materials such as Ti and Cr are widely used to increase adhesion of Au films and control their morphologies on the Si substrate. Simulations of these multi-layers on the Si substrate will have practical applications in the investigations of Au deposition on the Si substrate.

As discussed in Chapter 1, the deflection and surface stress of the gold-coated Si cantilever are influenced by the morphology of the Au film. The properties of the thin films can be influenced by the deposition rate, source power, film thickness, substrate and annealing temperature, and the tie layers between the deposited film and the substrate. Thus, by adjusting these factors during calculations, we can study the crystal growth and the surface stress of Au films under different conditions so as to theoretically find a deposition recipe that can produce more sensitive gold-coated sensors for molecular detections.

Bibliography

[1] R. Berger, Ch. Gerber, H.P. Lang, and J.K. Gimzewski. *Microelectr. Eng.*, 35:373–379, 1997.

[2] R. Berger, E. Delamarche, H. P. Lang, C. Gerber, J. K. Gimzewski, E. Meyer, and H. J. Guntherodt. *Science*, 276:2021–2024, 1997.

[3] M. Godin, P. J. Williams, V. Tabard-Cossa, O. Laroche, L. Y. Beaulieu, R. B. Lennox, and P. Grutter. *Langmuir*, 20:7090–7096, 2004.

[4] K. Oura and T. Hanawa. *Surf. Sci.*, 82:202–214, 1979.

[5] T. Narusawa, K. Kinoshita, W. M. Gibson, and A. Hiraki. *J. Vac. Sci. Technol.*, 18:872–875, 1981.

[6] B. Carrière, J. P. Deville, and A. El Maachi. *Surf. Sci.*, 168:149–157, 1986.

[7] K. Hricovini, J. E. Bonnet, B. Carrière, J. P. Deville, M. Hanbucken, and G. Le Lay. *Surf. Sci.*, 211/212:630–636, 1989.

[8] A. Taleb-Ibrahimi, C. A. Sebenne, D. Bolmont, and P. Chen. *Surf. Sci.*, 146:229–240, 1984.

[9] L. J. Brillson, A. D. Katnaniand M. Kelly, and G. Margaritondo. *J. Vac. Sci. Technol. A*, 2:551–555, 1984.

[10] Z. Imam, J. J. Metois, and G. Le Lay. *Surf. Sci.*, 162:628–633, 1985.

[11] S. L. Molodtsov, C. Laubschat, and G. Kaindl. *Phys. Rev. B*, 44:8850–8857, 1991.

[12] J. J. Yeh, J. Hwang, K. Bertness, D. J. Friedman, R. Cao, and I. Lindau. *Phys. Rev. Lett.*, 70:3768–3771, 1993.

[13] B. Lamontagne, E. Sacher, and M. R. Wertheimer. *Appl. Surf. Sci.*, 78:399–411, 1994.

[14] X. F. Lin and J. Nogami. *J. Vac. Sci. Technol. B*, 12:2090–2093, 1994.

[15] G. Yang, J. H. Kim, S. Yang, and A. H. Weiss. *Surf. Sci.*, 367:45–55, 1996.

[16] W.C.A.N. Ceelen, B. Moest, M. de Ridder, L. J. van IJzendoorn, A. W. Denier van der Gon, and H. H. Brongersma. *Appl. Surf. Sci.*, 134:87–94, 1998.

[17] J. H. Kim, G. Yang, S. Yang, and A. H. Weiss. *Surf. Sci.*, 475:37–46, 2001.

[18] M. S. Daw and M. I. Baskes. *Phys. Rev. Lett*, 50:1285–1288, 1983.

[19] J. H. Rose, J. R. Smith, Francisco Guina, and John Ferrante. *Phys. Rev. B*, 29:2963–2969, 1984.

[20] M. I. Basks. *Phys. Rev. Lett*, 59:2666–2669, 1987.

[21] M. I. Basks. *Phys. Rev. B*, 46:2727–2742, 1992.

[22] M. I. Baskes and R. A. Johnson. *Modelling Simul. Mater. Sci. Eng.*, 2:147–163, 1994.

[23] H. C. Huang, N. M. Ghoniem, J. K. Wong, and M. I. Baskes. *Model. Simul. Marer. Sci. Eng.*, 3:615–627, 1995.

[24] M. I. Baskes. *Mater. Chemist. and Phys.*, 50:152–158, 1997.

[25] Y. C. Yin X. Y. Yuan, K. Takahashi and T. Onzawa. *Model. Simul. Mater. Sci. Eng.*, 11:447–456, 2003.

[26] J. M. Zhang, F. Ma, and K. W. Xu. *Surf. Interface Anal.*, 35:662–666, 2003.

[27] Y. Mishin. *Acta Mater.*, 52:1451–1467, 2004.

[28] R. F. Zhang, L. T. Kong, H. R. Gong, and B. X. Liu. *J. Phys.: Condens. Matter*, 16:5251–5258, 2004.

[29] C. Kuo and P. Clancy. *Surf. Sci.*, 551:39–58, 2004.

[30] M. J. Puska, R. M. Nieminen, and M. Manninen. *Phys. Rev. B*, 24:3037–3047, 1981.

[31] M. S. Daw and M. I. Baskes. *Phys. Rev. B*, 29:6443–6453, 1984.

[32] S. M. Foils. *Phys. Rev. B*, 32:7685–7693, 1985.

[33] S. M. Foiles, M. I. Baskes, and M.S. Daw. *Phys. Rev. B*, 33:7983–7991, 1986.

[34] M. I. Basks, J. S. Nelson, and A. F. Wright. *Phys. Rev. B*, 40:6085–6100, 1989.

[35] M. I. Baskes, J.E.Angelo, and C.L.Bisson. *Modelling Simul. Mater. Sci. Eng.*, 2:505–518, 1994.

[36] W. H. Press, S. A. Teukolsky, V. T. Vetterling, and B. P. Flannery. *Numerical Recipes in Fortran 77: The Art of Scientific Computing.* Cambridge University Press, 1992.

[37] Q. Spreiter and M. Walter. *J. Comp. Phys.*, 152:102–119, 1999.

[38] R. Shuttleworth. *Proc. Phys. Soc. A*, 63:444–457, 1950.

[39] R. J. Needs and M. Mansfield. *J. Phys. Condens. Matter*, 1:7555–7563, 1989.

[40] G. J. Ackland and M. W. Finnis. *Philos. Mag. A*, 54:301–315, 1986.

[41] R. A. Johnson. *Phys. Rev. B*, 37:6121–6125, 1988.

[42] D. C. Rapaport. *The Art of Molecular Dynamics Simulation.* Cambridge University Press, United Kingdom, 2004.

[43] S. Narasimhan and M. Scheffler. *Zeitschrift fuer Physikalische Chemie*, 202:253–262, 1997.

[44] R. A. Wolkow. *Phys. Rev. Lett.*, 68:2636–2639, 1992.

[45] R. M. Tromp, R. J. Hamers, and J. E. Demuth. *Phys. Rev. Lett.*, 55:1303–1306, 1985.

[46] M. I. Baskes. *Modelling Simul. Mater. Sci. Eng.*, 5:149–158, 1997.

[47] P. Kruger and J. Pollmann. *Phys. Rev. Lett.*, 74:1155–1158, 1995.

[48] N. Roberts and R. J. Needs. *Surf. Sci.*, 236:112–121, 1990.

[49] B. N. Chapman. *Glow Discharge Processes.* John Willey and Sons , Inc, New York, 1980.

[50] W. C. A. N. Ceelen, M. de Ridder, B. Moest, and A.W. Denier van der Gon. *Surf. Sci.*, 430:146–153, 1999.

Appendix A

Abbreviations and Symbols

MEAM ..... the modified embedded atom method

EAM ..... the embedded atom method

cgm ..... conjugate gradient minimization

MD ..... molecular dynamics

E_i ..... the energy of atom i in the system

F_i ..... the embedding energy of atom i in the system

ρ_i ..... background electron density of atom i

φ_{ij} ..... pair potential between atom i and atom j

S_{ij} ..... screening function between atom i and atom j

N ..... total number of atoms in the system

E_{tot} ..... total energy of the system

A_i ..... fitting parameters in the embedding function

E_i^c ..... cohesive energy of atom i

Z_i ..... number of the nearest-neighbors of atom i

t_i ..... electron density weighting factors in Equation 2.4

ρ_i^e ..... electron density scaling factors in Equation 2.9

$\rho_i^{a(0)}$ ..... atomic electron density of atom i

β_i ..... parameters presenting the rate of electron density decaying

$\mathbf{C}$ ..... parameter to determine the ellipse for screening function

C_{min} ..... lower limit of C

C_{max} ..... upper limit of C

E_i^u ..... energy of atom i in the reference structure

r_i^e ..... nearest neighbor distance in the reference structure

B_i ..... bulk modulus of atom i

Ω_i ..... atomic volume of atom i

δ_i ..... parameters to adjust the repulsive and attractive energies in the MEAM potential

s_i ..... geometrical factors used when calculating the electron density in the reference structure

ΔE_{b-f} ..... structure energy difference between fcc and bcc structure

E_v^f ..... vacancy formation energy of the system

k_B ..... Boltzmann's constant

$\mathbf{T}$ ..... temperature of the system

σ ..... surface energy of the system

$\tau_{\alpha\beta}$ ..... elements of the surface stress tensor

$\epsilon_{\alpha\beta}$ ..... elements of the strain tensor

Δt ..... the time step in molecular dynamics simulations
1 time step = 0.4125 fs

Δ_{ij} ..... inter-layer relaxations between layer i and layer j

ML ..... monolayer

E_{pot} ..... potential energy of the system

E_k ..... kinetic energy of the system